

# Impact of grids and dynamical cores in CESM2.2 on the surface mass balance of the Greenland Ice Sheet

Adam R. Herrington<sup>1</sup>, Peter H. Lauritzen<sup>1</sup>, Marcus Lofverstrom<sup>2</sup>, William H. Lipscomb<sup>1</sup>, Andrew Gettelman<sup>1</sup> and Mark A. Taylor<sup>3</sup>

<sup>1</sup>National Center for Atmospheric Research, 1850 Table Mesa Drive, Boulder, Colorado, USA

<sup>2</sup>Department of Geosciences, University of Arizona, 1040 E. 4th Street, Tucson, Arizona USA

<sup>3</sup>Sandia National Laboratories, Albuquerque, New Mexico, USA

## Key Points:

- The CESM2.2 release includes several enhancements to the spectral-element dynamical core, including two Arctic refined mesh configurations.
- Quasi-uniform unstructured** grids degrade the Greenland Ice Sheet mass balance compared to latitude-longitude grids, **at the conventional 1° resolution**.
- The refined Arctic meshes substantially improve the surface mass balance over **conventional grid resolutions**.

15      **Abstract**

16      Six different configurations, a mixture of grids and atmospheric dynamical cores  
 17      available in the Community Earth System Model, version 2.2 (CESM2.2), are evaluated  
 18      for their skill in representing the climate of the Arctic and the surface mass balance of  
 19      the Greenland Ice Sheet (GrIS). The conventional  $1^\circ - 2^\circ$  resolution grids systemati-  
 20      cally overestimate both accumulation and ablation over the GrIS. Of these conventional  
 21      grids, the latitude-longitude grids outperform the quasi-uniform unstructured grids be-  
 22      cause they have more degrees of freedom to represent the GrIS. Two Arctic-refined meshes,  
 23      with  $1/4^\circ$  and  $1/8^\circ$  refinement over Greenland, are documented as newly supported con-  
 24      figurations in CESM2.2. The Arctic meshes substantially improve the simulated clouds  
 25      and precipitation rates in the Arctic. Over Greenland, these meshes skillfully represent  
 26      accumulation and ablation processes, leading to a more realistic GrIS surface mass bal-  
 27      ance. As CESM is in the process of transitioning away from conventional latitude-longitude  
 28      grids, these new Arctic-refined meshes improve the representation of polar processes in  
 29      CESM by recovering resolution lost in the transition to quasi-uniform grids, albeit at in-  
 30      creased computational cost.

31      **Plain Language Summary**

32      The mass balance of Earth's big ice sheets is crucially important for understand-  
 33      ing controls on global sea-level rise. However, the scale of the processes needed to rep-  
 34      resent ice sheet mass balance is challenging to resolve in conventional Earth System Mod-  
 35      els. This study evaluates the ability of different grids and atmospheric solvers (i.e., the  
 36      dynamical core) in CESM2.2 to resolve the surface mass balance (SMB) of the Green-  
 37      land Ice Sheet. We show that the ongoing transition away from latitude-longitude grids,  
 38      towards quasi-uniform unstructured grids in CESM2.2 leads to a degradation of the sim-  
 39      ulated SMB. Two variable-resolution grids with enhanced resolution over Greenland are  
 40      developed and incorporated into the release of CESM2.2, which substantially improves  
 41      the SMB over the latitude longitude grids.

42      **1 Introduction**

43      General Circulation Models (GCMs) are powerful tools for understanding the me-  
 44      teorology and climate of the high latitudes, which are among the most sensitive regions  
 45      on Earth to global and environmental change. GCMs differ vastly in their numerical treat-  
 46      ment of polar regions because of the so-called *pole problem* (Williamson, 2007). The pole  
 47      problem refers to numerical instability arising from the convergence of meridian lines into  
 48      polar singularities on latitude-longitude grids (e.g., Figure 1a, hereafter referred to as  
 49      *lat-lon* grids). Depending on the numerics, methods exist to suppress this instability, and  
 50      lat-lon grids may be advantageous for polar processes by representing structures with  
 51      finer resolution than elsewhere in the computational domain. With the recent trend to-  
 52      wards quasi-uniform unstructured grids, any potential benefits of lat-lon grids in polar  
 53      regions may be lost (hereafter, *quasi-uniform* refers to approximately isotropic grids, which  
 54      is not a characteristic of lat-lon grids, which are highly anisotropic). In this study, we  
 55      evaluate a number of grids and dynamical cores (hereafter referred to as *dycores*) avail-  
 56      able in the Community Earth System Model, version 2.2 (CESM2.2; Danabasoglu et al.,  
 57      2020), including new variable-resolution grids, to understand their impacts on the sim-  
 58      ulated Arctic climate. We focus specifically on the climate and surface mass balance of  
 59      the Greenland Ice Sheet.

60      In the 1970s, the pole problem was largely defeated through the adoption of effi-  
 61      cient spectral transform methods in GCMs (see Williamson, 2007, and references therein).  
 62      These methods transform grid point fields into a global, isotropic representation in wave  
 63      space, where linear operators (e.g., horizontal derivatives) in the (truncated) equation

set can be solved exactly. While spectral transform methods are still used today, local numerical methods have become desirable for their ability to run efficiently on massively parallel systems. The pole problem has thus re-emerged in contemporary climate models that use lat-lon grids, and some combination of reduced grids (modified lat-lon grids, with cells elongated in the longitudinal direction over the polar regions) and polar filters are necessary to ameliorate this numerical instability (Jablonowski & Williamson, 2011). Polar filters subdue the growth of unstable computational modes by applying additional damping to the numerical solution over polar regions. This damping reduces the effective resolution in polar regions such that the resolved scales are *approximately* the same everywhere on the grid. We emphasize *approximately*, since it is conceivable that marginal increases in effective resolution occur over polar regions in lat-lon grids, despite polar filtering, since resolved waves can be represented with more grid points than at lower latitudes.

Dycores built on lat-lon grids have some advantages over dycores built on unstructured grids. Lat-lon coordinate lines are orthogonal, and aligned with zonally symmetric circulations that characterize many large-scale features of Earth's atmosphere. Lauritzen et al. (2010) has experimented with rotating lat-lon models such that their coordinate lines no longer align with an idealized, zonally balanced circulation. For the finite-volume lat-lon dycore considered in this paper (hereafter *FV*), numerical errors were shown to be largest when the polar singularity is rotated into the baroclinic zone ( $45^{\circ}\text{N}$  latitude), generating spurious wave growth much earlier in the simulation than for other rotation angles. This illustrates the advantages of coordinate surfaces aligned with latitude bands, albeit an extreme example where the polar singularity and the polar filter are also contributing to the spurious wave growth. The unstructured grids all generate spurious baroclinic waves earlier in the simulations than the (unrotated) lat-lon models, although the unstructured model considered in this paper, the spectral-element dycore (hereafter *SE*), holds a balanced zonal flow without spurious wave growth appreciably longer than the rotated FV experiments (Lauritzen et al., 2010). And unlike FV, the SE dycore has the same error characteristics regardless of how the grid is rotated.

The polar filter in the FV model impedes efficiency at large processor (CPU) counts because it requires a spectral transform, which has a large communication overhead (Suarez & Takacs, 1995; Dennis et al., 2012). Unstructured grids support quasi-uniform grid spacing globally, and there is no pole problem (e.g., Figure 1c). This is in part why unstructured grids are becoming more common; their improved performance on massively parallel systems and lack of constraints on grid structure (Taylor et al., 1997; Putman & Lin, 2007; Wan et al., 2013). This increased grid flexibility allows for the adoption of variable-resolution grids (e.g., Figure 2; hereafter abbreviated as *VR*), sometimes referred to as regional grid refinement. In principle, grid refinement over polar regions can make up for any loss of resolution in transitioning away from lat-lon grids (e.g., Figure 2). However, local grid refinement comes at the cost of a smaller CFL-limited time step in the refined region; the CFL-condition — short for Courant–Friedrichs–Lewy condition — is a necessary condition for numerical stability when using discrete data in time and space.

We emphasize that the pole problem is a distinctive feature of the dycore in atmospheric models. Polar filters do not directly interfere with the physical parameterizations, nor do they have any bearing on the surface models; e.g., the land model can take full advantage of the greater number of grid cells in polar regions on lat-lon grids. This is particularly relevant for the surface mass balance (*SMB*; the integrated sum of precipitation and runoff) of the Greenland Ice Sheet, which relies on hydrological processes represented in the land model.

The SMB of the Greenland Ice Sheet (hereafter *GrIS*) is determined by processes occurring over a range of scales that are difficult to represent in GCMs (Pollard, 2010). GrIS precipitation is concentrated at the ice-sheet margins, where steep topographic slopes drive orographic precipitation. The truncated topography used by low resolution GCMs

enables moisture to penetrate well into the GrIS interior, manifesting as a positive precipitation bias (Pollard & Groups, 2000; van Kampenhout et al., 2018). GrIS ablation areas ([marginal regions where the annual SMB is negative](#)) are typically less than 100 km wide and are confined to low-lying areas or regions with low precipitation. These narrow ablation zones are not fully resolved in low-resolution GCMs, and may further degrade the simulated SMB. For example, CESM, version 2.0 (CESM2) underestimates ablation in the northern GrIS, leading to unrealistic ice advance when run with an interactive ice sheet component (Lofverstrom et al., 2020).

Regional climate models (RCMs) are commonly relied upon to provide more accurate SMB estimates. The limited area domain used by RCMs permits the use of high-resolution grids capable of resolving SMB processes, and can skillfully simulate the GrIS SMB (Box et al., 2004; Rae et al., 2012; Van Angelen et al., 2012; Fettweis et al., 2013; Mottram et al., 2017; Noël et al., 2018). However, unlike GCMs, RCMs are not a freely evolving system, and the atmospheric state must be prescribed at the lateral boundaries of the model domain. The inability of the RCM solution to influence larger-scale dynamics outside the RCM domain (due to the prescribed boundary conditions) severely limits this approach from properly representing the role of the GrIS in the climate system. In addition, the boundary conditions are derived from a separate host model, which introduces inconsistencies due to differences in model design between the host model and the RCM.

In order to retain the benefits of RCMs in a GCM, van Kampenhout et al. (2018) used the VR capabilities of the SE dycore in CESM, generating [grids](#) where Greenland is represented with [up to](#)  $1/4^\circ$  resolution, and elsewhere with the more conventional  $1^\circ$  resolution. The simulated SMB compared favorably to the SMB from RCMs and observations. The VR approach is therefore emerging as a powerful tool for simulating and understanding the GrIS and its response to different forcing scenarios.

The SE dycore has been included in the model since CESM version 1, but has been under active development ever since. This includes the switch to a dry-mass vertical coordinate (Lauritzen et al., 2018) and incorporation of an accelerated multi-tracer transport scheme (Lauritzen et al., 2017), made available in CESM2. This paper documents several additional enhancements to the SE dycore as part of the release of CESM2.2. These include three new VR configurations (Figure 2), two Arctic meshes and a Contiguous United-States mesh (**CONUS**; featured in Pfister et al. (2020)). While there are dozens of published studies using VR in CESM (e.g., Zarzycki et al., 2014; Rhoades et al., 2016; Gettelman et al., 2017; Burakowski et al., 2019; Bambach et al., 2021), these studies either used development code or collaborated closely with model developers. CESM2.2 is the first code release that contains out-of-the-box VR functionality.

This study compares the representation of Arctic regions using the SE and FV dycores in CESM2.2 (see description below), as these two dycores treat high latitudes (i.e., the pole problem) in different ways. Section 2 documents the grids, dycores, and physical parameterizations used in this study, and also describes the experiments, datasets, and evaluation methods. Section 3 analyzes the results of the experiments, and Section 4 provides a general discussion and conclusions.

## 2 Methods

CESM2.2 is a CMIP6-class (Coupled Model Intercomparison Project Phase 6; Eyring et al., 2016) Earth System Model maintained by the National Center for Atmosphere Research. CESM2.2 contains sub-component models for the atmosphere, land, ocean, sea-ice, and land-ice, and can be configured to run with varying degrees of complexity. All simulations described in this study use an identical transient 1979-1998 Atmospheric Model Inter-comparison Project (AMIP) configuration, with prescribed monthly sea-surface tem-

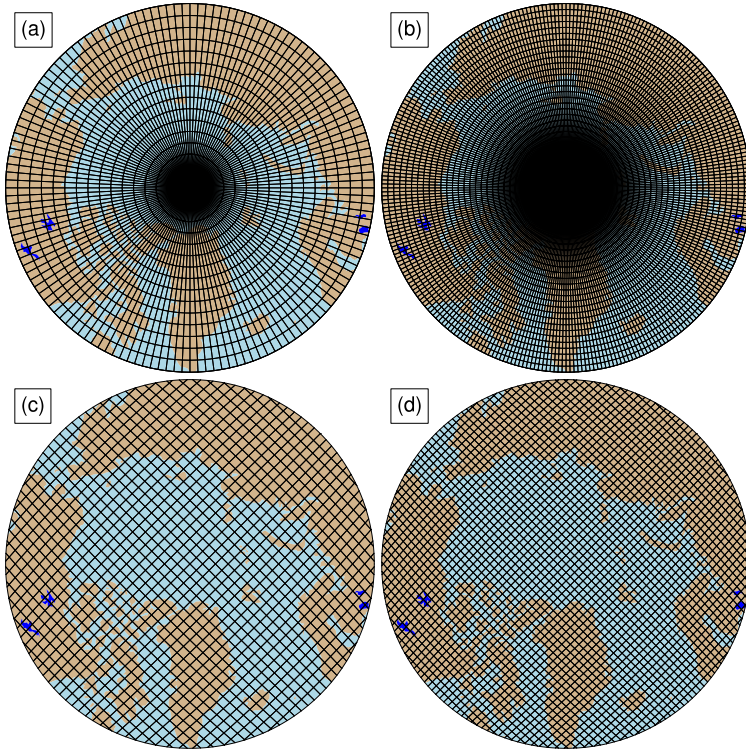


**Figure 1.** Computational grids for the  $1^\circ - 2^\circ$  lat-lon and quasi-uniform unstructured grids in this study. Grids names after Table 1, (a) f19, (b) f09, (c) ne30pg2 and (d) ne30pg3.

perature and sea ice following Hurrell et al. (2008). In CESM terminology, AMIP simulations use the FHIST computational set and run out of the box in CESM2.2. The land-ice component is not dynamically active in FHIST. However, the surface mass balance is computed by the land model before being passed to the land-ice component; FHIST includes the functionality to simulate the surface mass balance of the Greenland Ice Sheet.

## 2.1 Dynamical cores

The atmospheric component of CESM2.2 (Danabasoglu et al., 2020), the Community Atmosphere Model, version 6.3 (CAM6; Gettelman et al., 2019; Craig et al., 2021), supports several different atmospheric dynamical cores. These include dycores on lat-lon grids, such as finite-volume (FV; Lin, 2004) and Eulerian spectral transform (EUL; Collins et al., 2006) models, and dycores built on unstructured grids, including spectral-element (SE; Lauritzen et al., 2018) and finite-volume 3 (FV3; Putman & Lin, 2007) models. This study compares the performance of the SE and FV dycores, omitting the EUL and FV3 dycores. CESM2 runs submitted to CMIP6 used the FV dycore, whereas the SE dycore is often used for global high-resolution simulations (e.g., Small et al., 2014; Bacmeister & Coauthors, 2018; Chang et al., 2020) due to its higher throughput on massively parallel systems (Dennis et al., 2012).

### 2.1.1 Finite-volume (FV) dynamical core

The FV dycore integrates the hydrostatic equations of motion using a finite-volume discretization on a spherical lat-lon grid (Lin & Rood, 1997). The 2D dynamics evolve in floating Lagrangian layers that are periodically mapped to an Eulerian reference grid

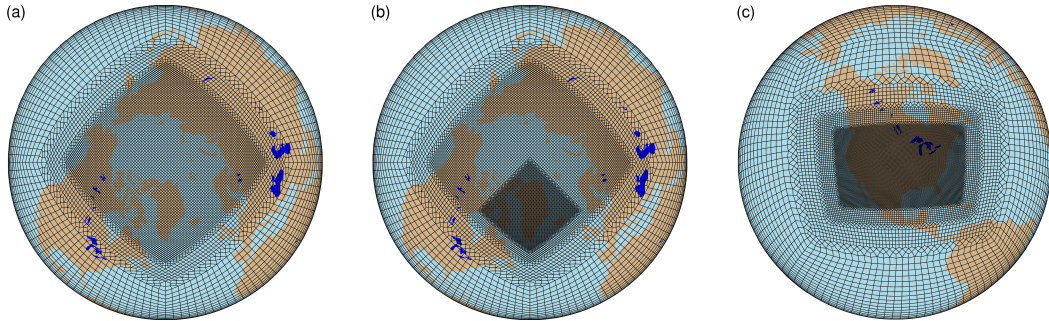


**Figure 2.** Variable-resolution grids available in CESM2.2, (a) **Arctic**, (b) **Arctic - GrIS** and (c) **CONUS**. Note what is shown is the element grid; the computational grid has  $3 \times 3$  independent grid points per element.

in the vertical (Lin, 2004). Hyperviscous damping is applied to the divergent modes, and is increased in the top few layers (referred to as a *sponge layer*) to prevent undesirable interactions with the model top, such as wave reflection (Lauritzen et al., 2011). A polar filter damps computational instability due to the convergence of meridians, permitting a longer time step. It takes the form of a Fourier filter in the zonal direction, with the damping coefficients increasing monotonically in the meridional direction (Suarez & Takacs, 1995). The form of the filter is designed to slow down the propagation of large zonal wave-numbers to satisfy the CFL condition of the shortest resolved wave at some reference latitude.

### 2.1.2 Spectral-element (SE) dynamical core

The SE dycore integrates the [hydrostatic](#) equations of motion using a high-order continuous Galerkin method (Taylor et al., 1997; Taylor & Fournier, 2010). The computational domain is a cubed-sphere grid tiled with quadrilateral elements (see Figure 2). Each element contains a fourth-order basis set in each horizontal direction, with the solution defined at the roots of the basis functions, the Gauss-Lobatto-Legendre quadrature points. This results in 16 nodal points per element, with 12 of the points lying on the (shared) element boundary. Communication between elements uses the direct stiffness summation (Canuto et al., 2007), which applies a numerical flux to the element boundaries to reconcile overlapping nodal values and produce a continuous global basis set.

As with the FV dycore, the dynamics evolve in floating Lagrangian layers that are subsequently mapped to an Eulerian reference grid. A dry mass vertical coordinate was recently implemented for thermodynamic consistency with condensates (Lauritzen et al., 2018). The 2D dynamics have no implicit dissipation, and so hyperviscosity operators are applied to all prognostic variables to remove spurious numerical errors (Dennis et al., 2012). Laplacian damping is applied in the sponge layer.

In CESM2.2, the SE numerics have been enhanced [relative to the CESM2.0 release](#) to mitigate spurious noise over topography. These algorithmic changes are described in Appendix A.

The SE dycore supports regional grid refinement via its VR configuration, requiring two enhancements over [quasi-uniform resolution grids](#). First, as the numerical viscosity increases with resolution, explicit hyperviscosity relaxes according to the local element size, reducing in strength by an order of magnitude per halving of the grid spacing. A tensor-hyperviscosity formulation is used (Guba et al., 2014), which adjusts the

coefficients in two orthogonal directions to more accurately target highly distorted quadrilateral elements. Second, the topography boundary conditions are smoothed in a way that does not excite grid scale modes, and so the NCAR topography software (Lauritzen et al., 2015) has been modified to scale the smoothing radius by the local element size, resulting in rougher topography in the refinement zone.

When using the SE dycore with quasi-uniform grid spacing, the SE tracer transport scheme is replaced with the Conservative Semi-Lagrangian Multi-tracer transport scheme (CSLAM) (Lauritzen et al., 2017). Atmospheric tracers have large, nearly discontinuous horizontal gradients that are difficult to represent with spectral methods, which are prone to oscillatory “Gibbs-ringing” errors (Rasch & Williamson, 1990). CSLAM has improved tracer property preservation and accelerated multi-tracer transport. It uses a separate grid from the spectral-element dynamics, dividing each element into  $3 \times 3$  control volumes with quasi-equal area. The physical parameterizations are computed from the state on the CSLAM grid, which has clear advantages over the original SE dycore in which the physics are evaluated at Gauss-Lobatto-Legendre points (Herrington et al., 2018). **CSLAM advection is not an available option in the VR configuration, which instead uses the standard SE tracer transport scheme with the physics evaluated at Gauss-Lobatto-Legendre points.**

## 2.2 Physical parameterizations

All simulations in this study use the CAM6 physical parameterization package (hereafter referred to as the *physics*; Gettelman et al., 2019). The physics in CAM6 differs from its predecessors through the incorporation of high-order turbulence closure, Cloud Layers Unified by Binormals (CLUBB; Golaz et al., 2002; Bogenschutz et al., 2013), which jointly acts as a planetary boundary layer, shallow convection, and cloud macrophysics scheme. CLUBB is coupled with the MG2 microphysics scheme (Gettelman & Morrison, 2015; Gettelman et al., 2015), which computes prognostic precipitation and uses classical nucleation theory to represent cloud ice for improved cloud-aerosol interactions. Deep convection is parameterized using a convective quasi-equilibrium mass flux scheme (Zhang & McFarlane, 1995; Neale et al., 2008) and includes convective momentum transport (Richter et al., 2010). Boundary layer form drag is modeled after Beljaars et al. (2004), and orographic gravity wave drag is represented with an anisotropic method informed by the orientation of topographic ridges at the sub-grid scale (the ridge orientation is derived from a high-resolution, global topography dataset (J. J. Danielson & Gesch, 2011)).

Initial simulations with the SE dycore produced weaker shortwave cloud forcing relative to the tuned finite-volume dycore in the standard CESM2 configuration. The SE dycore in CESM2.2 therefore has two CLUBB parameter changes to provide more realistic cloud forcing and top-of-atmosphere radiation balance. We reduced the width of the sub-grid distribution of vertical velocity (`clubb_gamma` = 0.308 → 0.270) and also reduced the strength of the damping for horizontal component of turbulent energy (`clubb_c14` = 2.2 → 1.6) to increase cloudiness. For a description of how CLUBB parameters impact the simulated climate, see Guo et al. (2015).

## 2.3 Grids

We evaluate model simulations on six different grids in this study (Table 1). The FV dycore is run with nominal  $1^\circ$  and  $2^\circ$  grid spacing, referred to as `f09` and `f19`, respectively (Figure 1a,b). We also run the  $1^\circ$  equivalent of the SE-CSLAM grid, referred to as `ne30pg3` (Figure 1d), where  $ne$  refers to a grid with  $ne \times ne$  quadrilateral elements per cubed-sphere face, and  $pg$  denotes that there are  $pg \times pg$  control volumes per element for computing the physics. We run an additional  $1^\circ$  SE-CSLAM simulation with the physical parameterizations computed on a grid with  $2 \times 2$  control volumes per el-

grid name	dycore	$\Delta x_{\text{eq}}$ (km)	$\Delta x_{\text{fine}}$ (km)	$\Delta t_{\text{phys}}$ (s)	25 nodes, cost	50 nodes, cost
f19	FV	278	-	1800	436.66	-
f09	FV	139	-	1800	1534.57	2024.24
ne30pg2	SE-CSLAM	167	-	1800	1497.26	1683.97
ne30pg3	SE-CSLAM	111	-	1800	1890.48	2090.43
ne30pg3*	SE-CSLAM	111	-	450	-	-
Arctic	SE	111	28	450	15947.41	16675.45
Arctic – GrIS	SE	111	14	225	40305.03	41036.67

**Table 1.** Grids and dycores used in this study.  $\Delta x_{\text{eq}}$  is the average equatorial grid spacing,  $\Delta x_{\text{fine}}$  is the grid spacing in the refined region (if applicable), and  $\Delta t_{\text{phys}}$  is the physics time step. FV refers to the finite-volume dycore, SE the spectral-element dycore, and SE-CSLAM the spectral-element dycore with CSLAM tracer advection. We use the ne30pg3 grid for two runs with different values of  $\Delta t_{\text{phys}}$ . The last columns provide the computational costs in core hours per simulated year (CHPSY). The costs are from single month runs using 25 nodes and 50 nodes on the Cheyenne supercomputer (Computational and Information Systems Laboratory, 2017).

ement, ne30pg2 (Figure 1c; Herrington et al., 2019, note CSLAM is still run on the  $3 \times 3$  control volume grid).

Three VR meshes were developed for the CESM2.2 release to support grid refinement over the Arctic and the United States (Figure 2). This paper serves as the official documentation of these grids. The VR meshes were developed using the software package SQuadgen (<https://github.com/ClimateGlobalChange/squadgen>). The Arctic grid is a  $1^\circ$  grid with  $1/4^\circ$  regional refinement over the broader Arctic region. The Arctic–GrIS grid is identical to the Arctic grid, but with an additional patch covering the island of Greenland with  $1/8^\circ$  resolution. The CONUS grid contains  $1/8^\circ$  refinement over the United States, and  $1^\circ$  everywhere else. The CONUS grid is not discussed any further in this paper; see Pfister et al. (2020) for simulations with the CONUS grid.

The accuracy of the simulated surface mass balance is expected to be sensitive to grid resolution. Figure 3a shows the average grid spacing over the Greenland Ice Sheet (*GrIS* hereafter) in all six grids, as well as two grids pertaining to the Regional Atmospheric Climate Model (RACMO; Noël et al., 2018, 2019), which are used for validation purposes in this study (Table 2). The ne30pg2 grid has the coarsest representation with an average grid spacing ( $\Delta x$ ) of  $\Delta x = 160$  km, and the Arctic – GrIS grid has the highest resolution with an average grid spacing of  $\Delta x = 14.6$  km, similar to the 11 km grid spacing of the RACMO2.3 grid. The ne30pg3 grid has an average  $\Delta x = 111.2$  km, substantially coarser than the f09 grid, with an average  $\Delta x = 60$  km. Although ne30pg3 and f09 have similar average grid spacing over the entire globe, and comparable computational costs, the convergence of meridians on the FV grid enhances the resolution over the GrIS. The Arctic grid has an average grid spacing of  $\Delta x = 27.8$  km.

The physics time step depends on the grid resolution. Increased horizontal resolution permits faster vertical velocities that reduce characteristic time scales, so the physics time step is reduced to avoid large time truncation errors (Herrington & Reed, 2018). The Arctic and Arctic – GrIS grids are run with a  $4\times$  and  $8\times$  reduction in physics time step relative to the default 1800 s time step used in the  $1^\circ$  and  $2^\circ$  grids (Table 1).

All grids and dycores in this study use 32 hybrid pressure-sigma levels in the vertical, with a model top of 2 hPa or about 40 km. However, any grid or dycore can in principle be run with a higher model top or finer vertical resolution.

## 2.4 Computational costs

The last columns of Table 1 provides cost estimates for the different grids and dycores. The costs, expressed as core hours per simulated year (CHPSY), are taken from single month runs of FHIST, with no i/o, and using 25 nodes (900 tasks) and 50 nodes (1800 tasks) on the Cheyenne supercomputer (Computational and Information Systems Laboratory, 2017). 25 nodes is on the low side for a typical multi-decadal climate simulation at  $1^{\circ}$  resolution, but it's the largest number of tasks that can be supported by the f19 grid, and we chose to fix the number of tasks across all grids for the purposes of comparing their costs. We also provide costs using 50 nodes, excluding f19, to provide a more practical cost estimate for longer climate integrations. There are probably better approaches for comparing costs across different grids and dycores, e.g., holding fixed the number of grid columns per task, but it is beyond the scope of this study.

The cheapest grid is the f19 grid at 436.66 CHPSY, as this is the only grid running with  $2^{\circ}$  dynamics. The f09 grid costs 1534.57 CHPSY using 25 nodes, which is noticeably cheaper than ne30pg3 at 1890.48 CHPSY. The ne30pg2 grid is 20% cheaper than the ne30pg3 grid, in both the 25 node and 50 node runs, consistent with previous estimates (Herrington & Reed, 2018). The FV model is known to be cheaper than SE at small core counts, whereas SE is more efficient than FV at large core counts due to its improved scalability (Dennis et al., 2005, 2012). In the more conventional 50 node runs, f09 costs are much more similar to ne30pg3, due to a 30% cost increase in f09 relative to the 25 node run (Table 1). The Arctic grid is an order of magnitude more expensive than the lat-lon and quasi-uniform grids, at about 16k CHPSY, whereas the Arctic–GrIS grid is a more than twice that (40k CHPSY). Note that all timing numbers are from runs without threading. The f09 grid is the only grid that runs out-of-the-box with threading; holding the number of tasks fixed leads to a 4%–6.5% reduction in CHPSY compared to runs without threading.

## 2.5 Simulated surface mass balance (SMB)

CESM simulates the GrIS SMB as the sum of ice accumulation and ice ablation. The latter contains contributions from sublimation and liquid runoff from ice melt. Liquid precipitation and liquid runoff may also contribute to ice accumulation by penetrating pore spaces in the snowpack/firn layer and freeze, forming ice lenses. These relevant SMB processes are represented by different CESM components, but it is the Community Land Model, version 5 (CLM; Lawrence et al., 2019), that aggregates these processes and computes the SMB.

CLM runs on the same grid as the atmosphere, and uses a downscaling technique to account for sub-grid variability in SMB. In short, the ice sheet patch in a CLM grid cell is subdivided into 10 elevation classes (ECs), each with a distinct surface energy balance and SMB. The area fraction of each EC is computed from the CISM initial conditions, which are based on a high-resolution dataset of the observed, modern extent and thickness of the GrIS (Morlighem et al., 2014). Note that for configurations with a dynamically active ice sheet, the area fractions are continuously updated throughout the run to reflect the evolving ice sheet geometry in CISM. The near-surface air temperature, humidity, and air density are calculated for each EC using an assumed lapse rate and the elevation difference from the grid-cell mean. Precipitation from CAM is repartitioned into solid or liquid based on the surface temperature of the EC; precipitation falls as snow for temperatures between  $T < -2^{\circ}$  C, as rain for  $T > 0^{\circ}$  C, and as a linear combination of rain and snow for temperatures between  $-2^{\circ}$  C and  $0^{\circ}$  C.

Changes in ice depth, not snow depth, count toward the SMB. Snow accumulation in each EC is limited to a depth of 10 m liquid water equivalent. Any snow above the 10 m cap contributes towards ice accumulation, and refreezing of liquid water within the snowpack is an additional source of ice. Surface ice melting (after melting of the overlying snow) yields a negative SMB. Integrating over all ECs, weighting by the area frac-

data product	years used in this study	resolution	citation
ERA5	1979-1998	1/4°	Copernicus (2019)
CERES-EBAF ED4.1	2003-2020	1°	Loeb et al. (2018)
CALIPSO-GOCCP	2006-2017	1°	Chepfer et al. (2010)
RACMO2.3	1979-1998	11 km	Noël et al. (2015)
RACMO2.3p2	1979-1998	5.5 km	Noël et al. (2019)

**Table 2.** Description of validation datasets used in this study.

tions, provides a more accurate SMB than would be found using the grid-cell mean elevation. For a more detailed description of how the SMB is computed in CESM, we refer the reader to Lipscomb et al. (2013); Sellevold et al. (2019); van Kampenhout et al. (2020); Muntjewerf et al. (2021).

Since snow in the accumulation zone must reach the cap to simulate a positive SMB, the snow depths on the VR grids were spun up by forcing CLM in standalone mode, cycling over data from a 20-year Arctic FHIST simulation for about 500 years. The 1°–2° lat-lon and quasi-uniform unstructured grids are initialized with the SMB from an existing f09 spun-up initial condition.

## 2.6 Validation Datasets

We use several validation datasets (Table 2) to assess the performance of the simulations. The ERA5 reanalysis product (Copernicus, 2019) is used for validating the large-scale circulation and extreme precipitation events. Clouds and radiation fields are validated using remote sensing products, the CERES-EBAF ED4.1 (Loeb et al., 2018) and the CALIPSO-GOCCP (Chepfer et al., 2010) datasets, respectively.

SMB datasets are gathered from multiple sources. RACMO, version 2.3 11km (RACMO23; Noël et al., 2015) and version 2.3p2 5.5km (RACMO2.3p2; Noël et al., 2018, 2019) are RCM simulations targeting Greenland, forced by ERA renalyses products at the domain's lateral boundaries. The RACMO simulations have been shown to perform skillfully against observations and are often used as modeling targets (e.g., Evans et al., 2019; van Kampenhout et al., 2020). The RACMO datasets are used along with the CERES-EBAF product to validate the radiative fluxes around Greenland.

In-situ SMB (snow pit and ice cores) and remote sensing datasets (e.g., IceBridge radar accumulation dataset) are maintained in The Land Ice Verification and Validation toolkit (LIVVkit), version 2.1 (Evans et al., 2019). However, these point-wise measurements are difficult to compare to model output spanning several different grids, especially since the SMB from each elevation class is not available from the model output. We used a nearest-neighbor technique for an initial analysis, which showed that the model biases are similar to those computed using the RACMO datasets. Because of the uncertainty of comparing gridded fields to point-wise measurements, and the lack of information added with regard to model biases, we omitted these datasets from our analysis.

## 2.7 SMB Analysis

We seek to integrate SMB components over a GrIS ice mask and to diagnose their contributions to the GrIS mass budget. However, the ice masks vary across the grids, especially in comparison to the RACMO3.2 ice mask, whose total area is about 3% less than that of the reference dataset (i.e., the GrIS initial conditions in CISIM; Figure 3b). CLM's dataset creation tool generates the model ice mask by mapping the reference dataset to the target grid using the Earth System Modeling Framework (ESMF) first-order conservative remapping algorithm (Team et al., 2021). The figure suggests that the map-

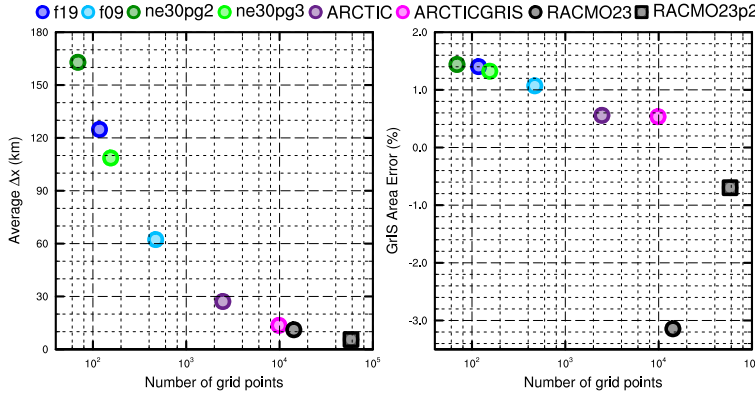


**Figure 3.** The spatial properties of the GrIS as represented by different grids in this study. (Left) GrIS area error, computed as the relative differences from a 4-km dataset used to create the CESM ice masks, (right) approximate average grid spacing over GrIS.

ping errors are less than 1.5% across the CESM2.2 grids. The area errors in Figure 3b may seem small, but even 1–2% area differences can lead to large differences in integrated SMB (Hansen et al., 2022).

We have taken a common-ice-mask approach by mapping all model fields to the lowest-resolution grids, i.e., the f19 and ne30pg2 grids, and integrating over these low-resolution ice masks. The use of low-resolution common ice masks is a conservative decision, and is justified because we seek to use first-order remapping algorithms to map fields to the common ice mask, which is not generally reliable when mapping to a higher-resolution grid than the source grid. We use two remapping algorithms: ESMF first-order conservative and the TempestRemap (Ullrich & Taylor, 2015) high-order monotone algorithm. Since mapping errors are sensitive to grid type, we evaluate all quantities on both common ice masks, the f19 and ne30pg2 masks. Thus, we evaluate an integrated quantity on a given grid up to four times to estimate the uncertainty due to differences in grid type and remapping algorithms.

The SMB is expressed in a form that is agnostic of water phase, a total water mass balance, to facilitate comparisons across different grids with different ice masks and to increase consistency with the variables available in the RACMO datasets. The SMB for total water can be expressed as:

$$SMB = accumulation + runoff + evaporation + sublimation, \quad (1)$$

where all terms have consistent sign conventions (positive values contribute mass, and negative values reduce mass). The accumulation source term refers to the combined solid and liquid precipitation, runoff refers to the liquid water sink, and evaporation/sublimation is the vapor sink. Since the runoff term aggregates many processes, we isolate the melting contribution by also tracking the combined melt of snow and ice.

The total water SMB (equation 1) is different from the SMB internally computed by CLM and described in section 2.5, which only tracks ice mass. We do not use CLM's internally computed SMB in this study. Rather, we utilize the components of the internally computed SMB to construct the total water SMB.

We consider two approaches for mapping and integrating the SMB components over the common ice masks:

- 421     1. Map the grid-cell mean quantities to the common grid, and integrate the mapped  
 422       fields over the common ice masks.  
 423     2. Map the patch-level quantities (i.e., the state over the ice fractional component  
 424       of the grid cell) to the common grid, and integrate the mapped fields over the com-  
 425       mon ice masks.

426     Note that we are mapping to low-resolution grids that have larger GrIS areas than  
 427       the source grids (Figure 3b). Since the components of equation 1 are not confined to the  
 428       ice mask, method 1 reconstructs the SMB over the portion of the common ice mask that  
 429       is outside the ice mask on the source grid. While this may be a an acceptable way to re-  
 430       construct the mass source terms over different ice masks, ice melt is zero outside the source  
 431       ice mask, and so method 1 will underestimate the mass sink term. This underestima-  
 432       tion is systematic in method 2, where all variables are exclusive to the ice mask; map-  
 433       ping to a lower-resolution grid will dilute a field of non-zero values over the ice mask with  
 434       a field of zeros outside the ice mask. However, patch-level values for processes exclusive  
 435       to the ice mask (e.g., ice melt) will on average have larger magnitudes than the grid-mean  
 436       quantities used in method 1.

437     The different error characteristics of the two methods are used to [further](#) diversify  
 438       the ensemble. Each of the four regridding combinations (with conservative and high-order  
 439       remapping to the **f09** and **ne30pg2** grids) are repeated with each method, resulting in  
 440       (up to) eight values for each integrated quantity. Unfortunately, the patch-level values  
 441       of evaporation/sublimation are not available from the model output, and we estimate  
 442       their contribution by zeroing out the field for grid cells that have no ice, prior to map-  
 443       ping to the common ice mask. This will degrade the SMB estimates using method 2, but  
 444       we are more interested in characterizing the behavior of individual processes across grids  
 445       and dycores, expressed as the components of the SMB, rather than the SMB itself.

### 446     3 Results

#### 447       3.1 Tropospheric temperatures

448     Before delving into the simulated Arctic climate conditions, we assess the global  
 449       mean differences between the various grids and dycores. Figure 4 shows 1979-1998 an-  
 450       nual mean, zonal mean height plots expressed as differences between [1°–2° lat-lon and](#)  
 451       [quasi-uniform unstructured](#) grids and dycores. The **f09** grid is warmer than the **f19** grid,  
 452       primarily in the mid-to-high latitudes throughout the depth of the troposphere. This is  
 453       a common response to increasing horizontal resolution in GCMs (Pope & Stratton, 2002;  
 454       Roeckner et al., 2006). Herrington and Reed (2020) have shown that this occurs in CAM  
 455       due to higher resolved vertical velocities which, in turn, generate more condensational  
 456       heating in the CLUBB macrophysics. The right panel in Figure 4a supports this inter-  
 457       pretation, showing an increase in the climatological CLUBB heating at all latitudes in  
 458       the **f09** grid, but with the largest increase in the mid-latitudes.

459     As the SE dycore is less diffusive than the FV dycore, the resolved vertical veloc-  
 460       ities are larger in the SE dycore, and so the **ne30pg3** troposphere is modestly warmer  
 461       than **f09** (Figure 4b). The stratosphere responds differently, with **ne30pg3** much cooler  
 462       than **f09** in the mid-to-high latitudes. Figure 4c also shows small temperature differences  
 463       between **ne30pg3** and **ne30pg2**, with **ne30pg3** slightly warmer near the tropopause at  
 464       high latitudes. This is consistent with the similar climates found for these two grids by  
 465       Herrington et al. (2019).

466     Comparing the VR grids to the [lat-lon and quasi-uniform](#) grids is complicated be-  
 467       cause we simultaneously increase the resolution and reduce the physics time-step, both  
 468       of which influence the solution (Williamson, 2008). We therefore run an additional **ne30pg3**  
 469       simulation with the shorter physics time step used in the **Arctic** grid (450 s), referred

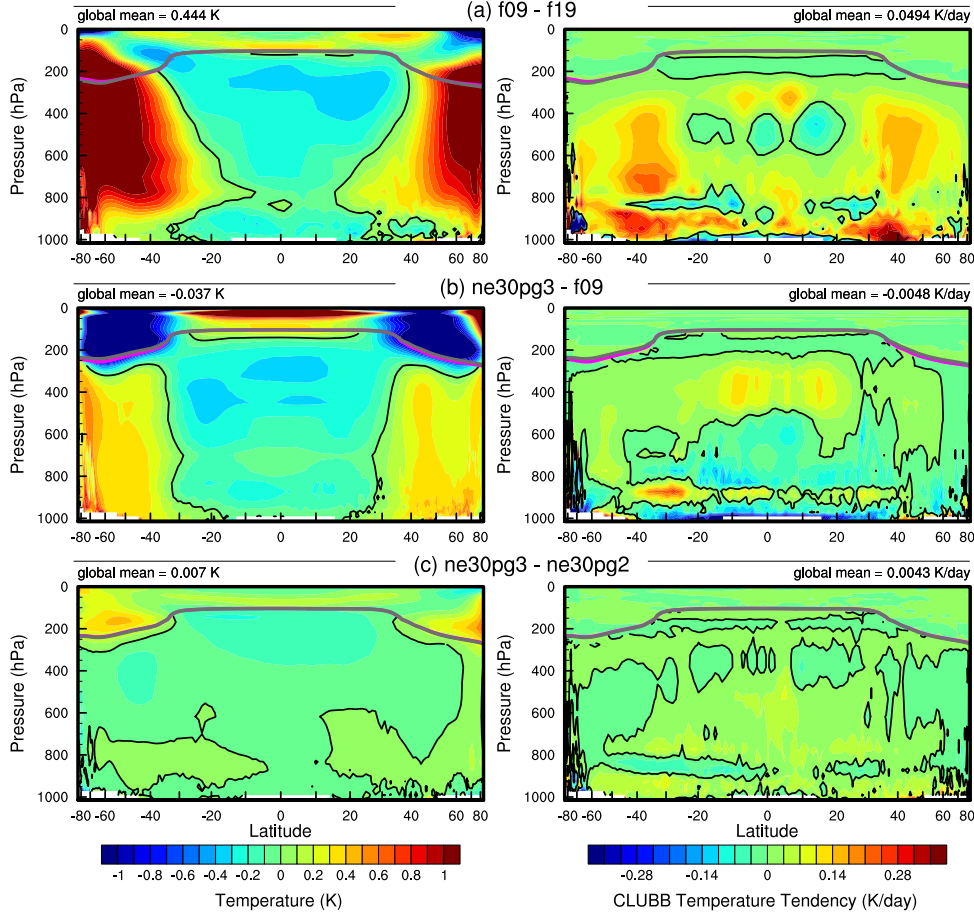


**Figure 4.** 1979–1998 annual mean temperature (left column) and CLUBB temperature tendencies (right column) in zonal mean height space, expressed as differences between the various  $1^\circ - 2^\circ$  grids. The thick grey and magenta lines are the tropopause for the control run and the test run, respectively.

to as `ne30pg3*` (Table 1). Figure 5a shows the difference between `ne30pg3*` and `ne30pg3` for climatological summer temperatures in zonal-mean height space. The troposphere is warmer with the reduced time step, and the mechanism is similar in that the shorter time step increases resolved vertical velocities (not shown) and CLUBB heating (right panel in Figure 5a). Figure 5b shows the difference in climatological summer temperature between the `Arctic` grid and the `ne30pg3*` grid. With the same physics time step, the greater condensational heating and warmer temperatures are confined to the refined Arctic region.

Figure 5c shows that the `Arctic-GrIS` grid is much warmer than the `Arctic` grid in the Arctic summer. This may be due, in part, to the shorter physics time step, but the temperature response is too large to be explained by enhanced condensational heating from CLUBB alone. This summer warming appears to be a result of variations in the stationary wave pattern, with a swath of anomalous southerly winds to the west of Greenland (not shown). This dynamic response is interesting, because other than the physics time step, the only difference between the `Arctic - GrIS` and `Arctic` runs is the doubling of resolution over Greenland. This behavior will be explored further in a future study.

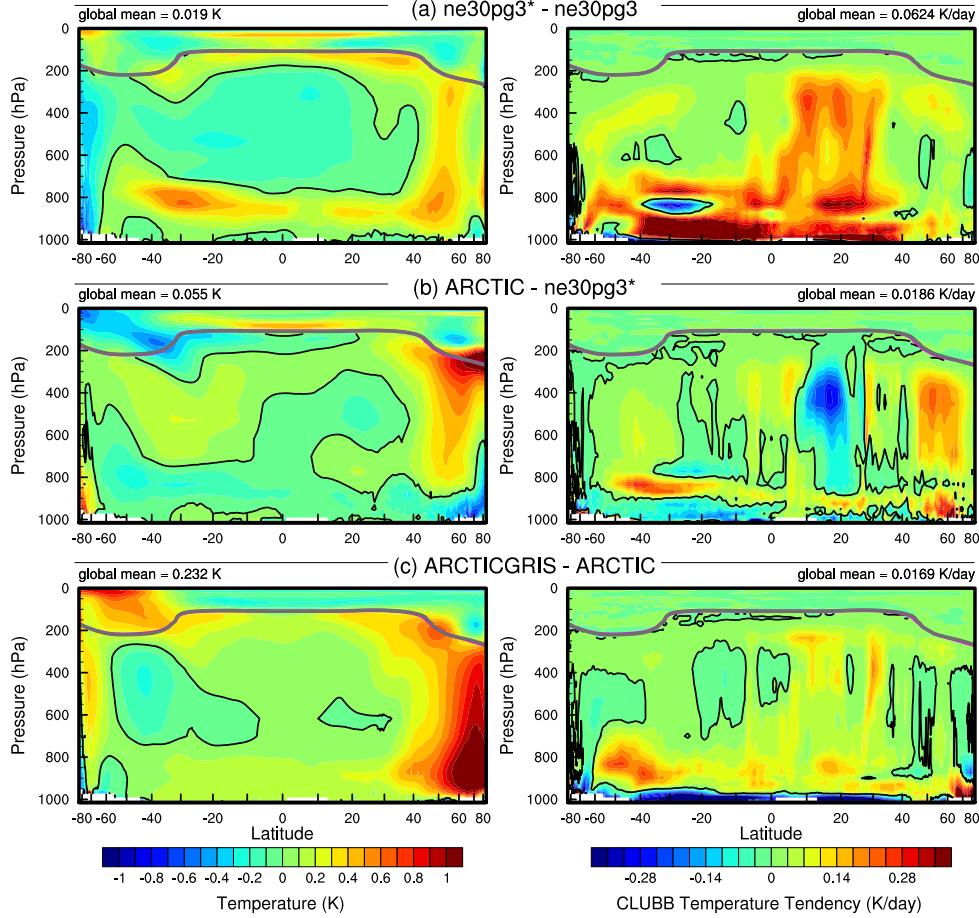


**Figure 5.** As in Figure 4 but for the short-time-step experiment and the VR grids. The fields plotted are for the climatological northern hemisphere summer. We focus on summer because that is when the resolution response is largest, and the refined regions are located in the northern hemisphere.

Keeping our focus on the Arctic region, and in particular Greenland, it is useful to understand summer temperature biases due to their control on ice and snow melt over the GrIS (Ohmura, 2001). Figure 6 shows the 1979–1998 lower troposphere summer temperature bias relative to ERA5, computed by equating a layer mean virtual temperature with the 500–1000 hPa geopotential thickness. The results are consistent with the zonal mean height plots; increasing resolution from f19 to f09 warms the climate, and the 1° SE grids are warmer than the FV grids. The FV summer temperatures are persistently colder than ERA5, whereas the 1° SE grids are not as cold, and are actually warmer than ERA5 at high-latitudes, north of 75°. All grids show a north-south gradient in bias over Greenland, with the summer temperature bias more positive for the northern part of the ice sheet. This pattern is also evident in the near surface temperature bias over Greenland (not shown).

The Arctic grid has summer temperatures similar to the 1° SE grids, but is slightly warmer over northern Eurasia and the North Pole (Figure 6). An anomalous cooling patch forms to the west of Greenland, centered over Baffin Island. The Arctic – GrIS grid

502 is warmer than the **Arctic** grid over most of the Arctic, but with a similar spatial pat-  
503 tern of summer temperature bias.

504 Some of these temperature differences may be related to differences in summer cloudi-  
505 ness. Figure 7 shows the summer shortwave cloud forcing bias in the six runs, using the  
506 CERES product. Shortwave cloud forcing quantifies the impact of clouds on shortwave  
507 radiation, taken as the difference between all-sky and clear-sky shortwave radiative fluxes  
508 at the top of the atmosphere. A negative bias corresponds to excessive reflection and cool-  
509 ing. The [lat-lon and quasi-uniform](#) grids have similar biases, with the clouds reflecting  
510 20–40 W/m<sup>2</sup> too much shortwave radiation over a wide swath of the Arctic, primarily  
511 the land masses. There is also a halo of positive bias (clouds not reflective enough) around  
512 the ocean perimeter of Greenland. The **Arctic** grid has much smaller cloud forcing bi-  
513 ases over the Arctic land masses, but is still too reflective over Alaska, the Canadian Archipelago,  
514 and parts of Eurasia. Compared to the **Arctic** grid, the **Arctic–GrIS** grid vastly re-  
515 duces the cloud forcing bias over Eurasia, and also improves the bias over North Amer-  
516 ica. In both VR grids, the halo of positive shortwave cloud forcing bias around the perime-  
517 ter of Greenland is absent.

518 The summer cloud forcing biases are consistent with the summer temperature bi-  
519 ases in Figure 6 – regions where clouds are too reflective coincide with regions that are  
520 too cold. While we have not quantified the contribution of cloud biases to the cooler Arc-  
521 tic temperatures, shortwave radiation is a crucial component of the Arctic energy bud-  
522 get during summer. The shortwave cloud forcing biases are on the order of 10 W/m<sup>2</sup>,  
523 which is a significant fraction of the total absorbed shortwave [radiation](#) during Arctic  
524 summer (Serreze et al., 2007) and is therefore likely a factor contributing to the cooler  
525 temperatures.

### 526 3.2 Clouds and precipitation over Greenland

527 In addition to summer temperatures, shortwave radiation is an important deter-  
528 minant of snow and ice melt. Figure 8 shows the summer incident shortwave radiation  
529 bias at the surface over Greenland and surrounding seas. The top panel shows the bias  
530 relative to the RACMO2.3p2 dataset, and the middle panel relative to the CERES dataset.  
531 The halo of excessive incident shortwave radiation around the coasts of Greenland is ap-  
532 parent for both datasets in relation to the coarser grids, consistent with the shortwave  
533 cloud forcing biases in Figure 7.

534 The ice sheet interior receives too little shortwave radiation in the coarser grids.  
535 On the VR grids, both the interior shortwave deficit and the excessive shortwave around  
536 the ocean perimeter are improved. This suggests that the coarse grid clouds are too thick  
537 in the interior of Greenland and too thin around the perimeter, which is consistent with  
538 the total summer cloud fraction bias, computed from the CALIPSO cloud dataset and  
539 shown in the bottom panel of Figure 8. Note that total cloud fraction characterizes the  
540 cloud field at all vertical levels, and attenuates the changes arising from any single layer  
541 due to the occurrence of overlapping clouds at other levels. The VR grids exhibit an over-  
542 all improvement in total cloud fraction bias, relative to the coarse grids.

543 The top panel of Figure 9 shows the annual climatological mean precipitation bias  
544 over the GrIS, expressed as the fractional difference from the RACMO2.3p2 solution. The  
545 coarse 1° – 2° grids have large, positive biases centered over the southern dome. The  
546 **Arctic** grid reduces this bias substantially, and the **Arctic–GrIS** grid reduces it fur-  
547 ther, with precipitation centers migrating from the interior toward the margins.

548 The more accurate representation of orographic precipitation in the VR grids is con-  
549 sistent with the cloud and radiation biases, cf. Figures 7, 8, and 9. The agreement of the  
550 cloud, radiation and precipitation biases in and around Greenland from multiple inde-  
551 pendent datasets indicates that the biases are a robust feature of the coarser grids. The

grid name	accumulation	total melt	runoff	sublimation	SMB
RACMO	681.7 (733.5)	-318.6 (-436.4)	-189.1 (-258.5)	-34.5 (-38.8)	458.1 (436.2)
ne30pg2	1007. (973.4)	-519.9 (-647.3)	-381.9 (-347.0)	-33.9 (-32.1)	591.2 (594.3)
ne30pg3	931.0 (909.3)	-540.8 (-686.7)	-375.8 (-330.1)	-34.1 (-32.6)	521.2 (546.6)
f19	884.9 (913.5)	-414.0 (-546.5)	-284.0 (-284.3)	-36.5 (-37.5)	564.4 (591.7)
f09	873.9 (882.1)	-389.1 (-482.3)	-256.1 (-212.3)	-37.3 (-37.4)	580.5 (632.4)
Arctic	784.1 (818.6)	-335.5 (-436.8)	-215.8 (-194.2)	-42.4 (-43.9)	526.0 (580.5)
Arctic – GrIS	693.8 (747.3)	-437.3 (-610.4)	-276.8 (-307.8)	-48.1 (-51.8)	369.0 (387.7)

**Table 3.** 1979-1998 surface mass balance of the Greenland Ice Sheet in Gt/yr. Values shown are using the common ice mask approach described in the methods section, whereas values in parentheses are from integrating over the native grid and ice mask.

552 reduced biases in the VR grids suggest that the deficiencies of the coarse grids are due  
 553 to insufficient horizontal resolution, consistent with previous findings that coarse GCMs  
 554 have large, positive precipitation biases over Greenland (Pollard & Groups, 2000; van  
 555 Kampenhout et al., 2018).

### 556 3.3 Greenland surface mass balance

557 Table 3 shows the 1979-1998 climatological SMB components for each grid, com-  
 558 pared with RACMO. The values in the table are averages over the ensemble of mapping  
 559 methods to the common ice masks described in section 2.7, and the RACMO values re-  
 560 fer to the average of both RACMO ensembles. Table 3 also contains (in parenthesis) the  
 561 SMB components derived from evaluating the integrals on each model’s native grid and  
 562 ice mask. Of note is the large reduction in melt rates compared to the values computed  
 563 on the native grid, illustrating the dissipation of this quantity discussed in section 2.7.  
 564 For integrated precipitation, the differences between the native and common ice mask  
 565 approaches are much smaller, since the combined solid/liquid precipitation rates are not  
 566 directly tied to the ice mask.

567 The coarse grids are characterized by too much precipitation and too much melt-  
 568 ing and runoff, compared with RACMO. The total SMB on coarse grids therefore has  
 569 smaller errors than the individual components (Table 3), because large errors in the source  
 570 and sink terms offset one another when added together. Such compensating errors un-  
 571 derline the importance of understanding the extent to which a model is getting the right  
 572 SMB for the right reasons.

573 Figure 10 shows time series of annually integrated precipitation and snow/ice melt  
 574 over the GrIS for the various different grids and dycores, and RACMO in black. The 1979-  
 575 1998 climatological mean values from Table 3 are shown as circles on the right side of  
 576 the panels. The [1°–2° lat-lon](#) and [quasi-uniform](#) grids have positive precipitation bi-  
 577 ases, whereas the VR grids have the smallest biases, with precipitation comparable to  
 578 RACMO. The f19 and f09 grids perform similarly, with +110 Gt/yr bias, whereas ne30pg3  
 579 is biased by about +165 Gt/yr and ne30pg2 by +230 Gt/yr.

580 The combined annual snow/ice melt shown in the bottom panel of Figure 10 in-  
 581 dicates that the Arctic grid simulates the most realistic melt rates, with the other grids  
 582 having more melt than RACMO. The Arctic–GrIS grid over-predicts melting by about  
 583 125 Gt/yr. This is likely due to an anomalously warm lower troposphere during the sum-  
 584 mer, relative to the Arctic run (Figure 6). The f19 and f09 melting rates are improved  
 585 over Arctic–GrIS, overestimating melt by only 70–90 Gt/yr. The SE grids have the  
 586 largest positive melt bias, between 200–220 Gt/yr.

To illustrate the regional behavior of the SMB components, Figure 11 shows the precipitation and combined snow/ice melt integrated over the basins defined by Rignot and Mouginot (2012). The uncertainty due to differences in basin area is larger than for GrIS-wide integrals, owing to the differences in basin boundaries on the common ice masks, which are shown in the f19 and ne30pg2 panels of Figure 9. Nonetheless, the regional totals in Figure 11 correctly show the southeast and southwest basins have the most accumulation. In all basins, accumulation decreases monotonically with increasing grid resolution, though with some exceptions. The **Arctic–GrIS** grid simulates less precipitation than RACMO in the central-east and southeast basins, and is closest of all grids to RACMO in the large southwest basin.

The basin-integrated melt rates in Figure 11 depend on the dycore. The quasi-uniform SE grids have the largest positive biases in all basins. The **Arctic–GrIS** grid is a close second, while the FV grids have systematically smaller melt-rates and melt-rate biases. The “second-place” standing of **Arctic–GrIS** is somewhat unexpected, as this grid has the warmest lower-troposphere summer temperatures (Figure 6) and greatest incident shortwave radiation (Figure 8), yet it has less melting than the quasi-uniform SE grids.

Lower troposphere temperature is not a strict proxy for melting; e.g., it may not capture microclimate effects as a result of a better representation of the low-elevation ablation zones. The Positive Degree-Day temperature-based melt index (PDD; Braithwaite, 1984), which accumulates the near-surface temperature in  $^{\circ}\text{C}$  for days with temperature above freezing, is a more accurate proxy for melting. PDD is nonlinear in mean monthly temperature (Reeh, 1991). We compute PDD from monthly mean 2-meter temperature using the method of Calov and Greve (2005), assuming a fixed monthly mean standard deviation of  $3^{\circ}\text{C}$  and a degree-day factor of  $5 \text{ mm d}^{-1} ^{\circ}\text{C}^{-1}$ . This specific degree-day factor lies between typical values reported for snow and ice, in order to easily apply the PDD method to estimate the combined snow and ice melt.

Figure 11c shows the basin-integrated PDD melt estimate. In the large southeast and southwest basins (and all the other western basins), the ne30pg3 grid has larger PDD-based melt than the **Arctic–GrIS** grid. The FV grids also have large PDD-based melt in the southwest basin, relative to **Arctic–GrIS**. The PDD plots indicate that the relationship between temperature and melt is not well approximated by the summer lower-troposphere temperatures in Figure 6.

The bottom panel of Figure 9 presents the biases in the combined ice/snow melt as map plots. These plots show that the largest melt biases are on the southeast and northwest coasts, where large coarse-grid cells overlap with the ocean. One possibility is that these problematic grid cells are situated at lower elevations than the true ice sheet surface, leading to a warm bias and too much melt. Figure 12 shows the representation of the ice sheet surface along two transects on the different grids, compared to the high-resolution dataset used to generate CAM topographic boundary conditions (J. Danielson & Gesch, 2011; Lauritzen et al., 2015). The two transects are shown in Figure 9: the east-west “K-transect” in southwest Greenland and a transect extending from the central dome down to the Kangerlussuaq glacier on the southeast coast. The  $1^{\circ}$ – $2^{\circ}$  grids are noticeably coarse, with only a handful of grid cells populating the transect. The f09 grid is a bit of an exception since the grid cells narrow in the zonal direction at high latitudes, and so a larger number of grid cells fit into the east-west transects. The VR grids more accurately reproduce the steep margins of the ice sheet, capturing the characteristic parabolic shape of the GrIS margin.

The transects in Figure 12 show that the ice sheet surface on the coarse grids is not systematically lower than the true surface in ablation zones. Rather, the smoothing and flattening of the raw topography, necessary to prevent the model from exciting grid-scale numerical modes, causes the lower-elevation ablation zones to extend beyond the true ice sheet margin, causing the modeled ablation zones (which must reside within

the ice sheet mask) to be elevated relative to the actual ice surface. The **f19** grid has both the smoothest topography and the flattest ice sheet since its dynamics are coarsest, whereas the **f09**, **ne30pg2** and **ne30pg3** grids have similar dynamical resolution and use identical smoothing. This suggests that coarser models will tend to elevate the ablation zones [relative to where they should be, which may be expected to cause anomalous \(adiabatic\) cooling and](#) depressed melt rates, but this is opposite the melt bias that occurs in the coarse grid simulations.

Figure 12 also shows the ice margin boundary, illustrating that the ablation zone lies in a narrow horizontal band where the ice sheet rapidly plunges to sea-level. Due to this abrupt transition, coarse grids will commonly represent the ablation zone with grid cells containing mixtures of ice-covered and ice-free regions. We hypothesize that coarser models have larger melt biases because summer melting is confined to these mixed ice/land/ocean grid cells. CLM deals with land heterogeneity in a complex and sophisticated manner, but CAM only sees the homogenized state after [area](#) averaging over the sub-grid mixture. Thus, warm ice-free land patches in a grid cell may unduly influence the climate over the entire grid cell, causing a warm bias over the ice-covered patch [and more melting](#).

Figure 13 shows the mean melt bias, relative to both RACMO datasets, conditionally sampled based on grid cell ice fraction in the GrIS region. Errors are computed after mapping the melt rates to the common ice masks using different methods, described in section 2.7. The grid cell ice fractions therefore pertain to ice fractions on the low-resolution common ice masks. Also shown are the  $\pm 1$  standard deviation of the biases for each bin. The figure shows that coarser grids can be characterized by a monotonic increase in melt bias as the grid cell ice fraction decreases. The VR grids have the smallest melt biases for small grid cell ice fractions (smaller than 50%), the [quasi-uniform](#) SE grids and **f19** have the largest melt biases and the **f09** grid melt biases lie between these two cases. Figure 13 generally supports our hypothesis that the prevalence of mixed-grid cells in the ablation zone of coarse grids is responsible for their large melt bias.

### 3.4 Precipitation extremes

Synoptic storms are tracked using TempestExtremes atmospheric feature detection software (Ullrich et al., 2021). As the **Arctic** grid contains  $1/4^\circ$  refinement north of about  $45^\circ$  latitude, the storm tracker is applied to this region for the **Arctic** and **ne30pg3** runs to identify differences in storm characteristics due to horizontal resolution.

Figure 14 shows monthly PDF ([probability density function](#)) of the precipitation rates associated with storms. The PDFs are constructed by sampling all the precipitation rates within  $30^\circ$  of the storm center, for each point on the storm track and for all storms. The PDFs are evaluated on an identical composite grid for all runs, and so storm statistics are not impacted by differences in output resolution. The **Arctic** run has larger extreme precipitation rates compared to **ne30pg3** in every month, but the increase is greatest in the summer months, which coincides with the most extreme events of the year. This is primarily due to increased resolution and not the reduced physics time step; the **ne30pg3\*** run only marginally increases the extreme precipitation rates compared with **ne30pg3** (Figure 14).

The extreme precipitation rates in the **Arctic** run are closer than **ne30pg3** to the ERA5 reanalysis (Figure 14). It is difficult to know how much the extreme precipitation rates in ERA5 are constrained by data assimilation, or whether these precipitation rates are due to using a similar  $1/4^\circ$  model as the **Arctic** grid. However, it is well documented that  $1/4^\circ$  models are more skillful at simulating extreme events (Bacmeister et al., 2013; Obrien et al., 2016). A more realistic representation of extreme precipitation events is an additional benefit of the VR grids.

689 

## 4 Conclusions

690 Running CESM2.2 in an AMIP-style configuration, we have evaluated six grids from  
 691 two dynamical cores for their performance over the Arctic and in simulating the GrIS  
 692 SMB. The  $1 - 2^\circ$  finite-volume grids have enhanced resolution over polar regions due  
 693 to their convergence of meridian lines, although a polar filter is used to prevent spuri-  
 694 ous atmospheric features from forming in these regions. SE grids comparable to the res-  
 695 olution of the FV grids have an isotropic grid structure where the grid resolution is sim-  
 696 ilar over the entire model domain. We developed two VR grids and introduced them into  
 697 CESM2.2 as part of this work. Both use the SE dycore; the **Arctic** grid has  $1/4^\circ$  refine-  
 698 ment over the broader Arctic, whereas the **Arctic – GrIS** grid is identical except for  
 699 a  $1/8^\circ$  patch of refinement over Greenland. A third VR grid, **CONUS**, with  $1/8^\circ$  refine-  
 700 ment over the **US**, has also been made available in CESM2.2.

701 In general, the FV grids have colder summer temperatures over the Arctic com-  
 702 pared with the SE grids (including the VR grids). The cloud biases in all the **lat-lon and**  
 703 **quasi-uniform** resolution grids, whether FV or SE, are similar, in general being too cloudy  
 704 over Arctic land masses. It should be emphasized that our analysis is specific to the Ar-  
 705 ctic summer because of its relevance to GrIS melt rates. An improved representation of  
 706 clouds in the Arctic does not imply improved clouds at lower latitudes.

707 At the regional level, there is a halo of negative cloudiness bias around the ocean  
 708 perimeter of Greenland on all  $1 - 2^\circ$  grids, but not the VR grids. This negative cloud  
 709 bias contrasts with a positive cloud bias over the ice sheet interior. This anomaly pat-  
 710 tern is attributed to deficient orographic precipitation in the coarser model grids. With  
 711 overly smooth topography on the  $1 - 2^\circ$  grids, synoptic systems moving into Greenland  
 712 are not sufficiently lifted when encountering the steep ice margins. As a result, excess  
 713 precipitation falls in the GrIS interior, instead of being concentrated on the steep coastal  
 714 margins as shown by observations (Pollard & Groups, 2000; van Kampenhout et al., 2018).  
 715 This results in a positive precipitation and cloud bias in the ice sheet interior, and a halo  
 716 of low cloud bias about the perimeter. The agreement of different observational data prod-  
 717 ucts on this bias lends confidence in the attribution of causes. The VR grids compare  
 718 better to the observations and show that orographic precipitation in Greenland is largely  
 719 resolved when the horizontal resolution is increased sufficiently.

720 We integrated the primary source and sink terms of the SMB equation over the GrIS  
 721 for each of the six grids. The  **$1^\circ - 2^\circ$  lat-lon and quasi-uniform** grids have large posi-  
 722 tive accumulation biases because they fail to resolve orographic precipitation. The quasi-  
 723 uniform SE grids have larger accumulation biases, suggesting that the FV grids are more  
 724 skillful for precipitation due to finer resolution over Greenland, and despite a polar fil-  
 725 ter. The VR grids have the most accurate accumulation rates of all the grids. The pri-  
 726 mary mass sink term of the GrIS, ice/snow melt, has similar biases; the coarse grids melt  
 727 too much, with a greater bias for quasi-uniform SE grids. In general, on coarse grids, er-  
 728 rors in the individual SMB terms are larger than the errors in the SMB itself, due to com-  
 729 pensating errors. This observation serves as a precaution; projecting mass-loss from a  
 730 glacier or ice sheet cannot be reliable if the processes representing the components of the  
 731 SMB are incorrect from the start, even if the total SMB has the right magnitude.

732 The **Arctic – GrIS** grid has the warmest summer lower troposphere of all grids,  
 733 yet it has less melting than the quasi-uniform resolution SE grids. This suggests that  
 734 grid resolution is somehow contributing to the melt biases in coarse grids, in a way that  
 735 is not obvious from the large-scale dynamics. We propose a mechanism: coarse grids rep-  
 736 resent ablation zones using grid cells with mixed surface types, ice-covered and ice-free.  
 737 The warmer ice-free patches may largely determine the mean state, leading to a warm  
 738 bias over the ice-covered patches of the grid cell. This mechanism is supported by anal-  
 739 ysis of melt biases binned by grid-cell ice fraction.

740 The **Arctic** grid substantially improves the simulated Arctic climate, including pre-  
 741 precipitation extremes and the GrIS SMB, compared to the **1°–2° lat-lon and quasi-uniform**  
 742 grids. The **Arctic–GrIS** grid has the most realistic cloud and precipitation fields, but  
 743 its summer temperatures are too warm. The 1° FV model gives a surprisingly realistic  
 744 SMB, likely due to the relatively fine resolution of Greenland on lat-lon grids (but per-  
 745 haps also because it is the most heavily tuned model configuration in CESM). In par-  
 746 ticular, a greater number of grid cells in the ablation zone reduces the influence of mixed  
 747 ice-covered/ice-free grid cells that represent ablation poorly on the other **lat-lon and quasi-**  
 748 **uniform** grids.

749 As modeling systems move away from lat-lon grids towards quasi-uniform unstruc-  
 750 tured grids, it is worth taking stock of whether this will degrade the simulated polar cli-  
 751 mate. We have found that the 1° FV model has clear advantages over the 1° SE model  
 752 for simulating the GrIS SMB. That is, the simulated GrIS SMB will be adversely im-  
 753 pacted in future CESM versions, after the FV dycore is phased out. This finding will not  
 754 interrupt the ongoing transition towards unstructured grids in CESM, which is largely  
 755 driven by gains in computational efficiency and grid refinement capabilities. We there-  
 756 fore provide the Arctic refined-meshes to the community by way of CESM2.2, provid-  
 757 ing users the option to simulate a more realistic GrIS SMB, although at a substantial  
 758 computational premium relative to conventional 1° – 2° grids.

759 We are working to develop a configuration of the **Arctic** grid that is fully-coupled  
 760 with the CESM ocean and sea ice components and the Community Ice Sheet Model (CISM),  
 761 to provide multi-century projections of the state of the GrIS and its contribution to sea-  
 762 level rise. We have also developed a visualization of the **Arctic–GrIS** run, now avail-  
 763 able on youtube (see link in Acknowledgements) to increase awareness of the capabili-  
 764 ties of CESM2.2. Figure 15 shows a snapshot of this visualization, illustrating mesoscale  
 765 katabatic winds descending the southeastern slopes of the GrIS. These new grids and con-  
 766 figurations will provide new opportunities for CESM polar science, and they aim to con-  
 767 tribute to an improved understanding of the polar environment. However, we recognize  
 768 the potentially prohibitive costs for some users, and so will continue to explore differ-  
 769 ent grids, parameterizations and workflows that can provide some of the same benefits  
 770 of the VR grids, but at a lower cost.

## 771 **Appendix A Details on spectra-element dynamical core improvements 772 since the CESM2.0 release**

773 Since the CESM2.0 release of the spectral-element dynamical core documented in  
 774 Lauritzen et al. (2018) some important algorithmic improvements have been implemented  
 775 and released with CESM2.2. These pertain mainly to the flow over orography that, for  
 776 the spectral-element dynamical core, can lead to noise aligned with the element bound-  
 777 aries (Herrington et al., 2018).

### 778 **A1 Reference profiles**

779 Significant improvement in removing noise for flow over orography can be achieved  
 780 by using reference profiles for temperature and pressure

$$T^{(ref)} = T_0 + T_1 \Pi^{(ref)}, \quad (A1)$$

$$p_s^{(ref)} = p_0 \exp \left( -\frac{\Phi_s}{R^{(d)} T_{ref}} \right), \quad (A2)$$

781 (Simmons & Jiabin, 1991) where  $g$  gravity,  $T_1 = \Gamma_0 T_{ref} c_p^{(d)} / g \approx 192K$  with standard  
 782 lapse rate  $\Gamma_0 \equiv 6.5K/km$  and  $T_0 \equiv T_{ref} - T_1 \approx 97K$ ;  $T_{ref} = 288K$  ( $c_p^{(d)}$  specific heat  
 783 of dry air at constant pressure;  $R^{(d)}$  gas constant for dry air), and  $\Phi_s$  surface geopoten-

784      tial. The reference Exner function is

$$\Pi^{(ref)} = \left( \frac{p^{(ref)}}{p_0} \right)^\kappa \quad (A3)$$

785      where  $\kappa = \frac{R^{(d)}}{c_p^{(d)}}$ . The reference surface pressure  $p_0 = 1000\text{hPa}$  and at each model level  
786      the reference pressure  $p^{(ref)}$  is computed from  $p_s^{(ref)}$  and the standard hybrid coefficients

$$p^{(ref)}(\eta) = A(\eta)p_0 + B(\eta)p_s^{(ref)}, \quad (A4)$$

787      where  $A$  and  $B$  are the standard [hybrid](#) coefficients (using a dry-mass generalized ver-  
788      tical mass coordinate  $\eta$ ). These reference profiles are subtracted from the prognostic tem-  
789      perature and pressure-level-thickness states before applying hyperviscosity:

CESM2.0 → CESM2.2

$$\nabla_\eta^4 T \rightarrow \nabla_\eta^4 \left( T - T^{(ref)} \right), \quad (A5)$$

$$\nabla_\eta^4 \delta p^{(d)} \rightarrow \nabla_\eta^4 \left( \delta p^{(d)} - \delta p^{(ref)} \right). \quad (A6)$$

790      This reduces spurious transport of temperature and mass up/down-slope due to the hy-  
791      perviscosity operator.

## 792      A2 Rewriting the pressure gradient force (PGF)

793      In the CESM2.0 the following (standard) form of the pressure gradient term was  
794      used:

$$\nabla_\eta \Phi + \frac{1}{\rho} \nabla_\eta p, \quad (A7)$$

795      where  $\Phi$  is geopotential and  $\rho = \frac{R^{(d)} T_v}{p}$  is density (for details see Lauritzen et al., 2018).  
796      To alleviate noise for flow over orography, we switched to an Exner pressure formulation  
797      following Taylor et al. (2020), which uses that (A7) can be written in terms of the Exner  
798      pressure

$$\nabla_\eta \Phi + c_p^{(d)} \theta_v \nabla_\eta \Pi, \quad (A8)$$

799      where the Exner pressure is

$$\Pi \equiv \left( \frac{p}{p_0} \right)^\kappa. \quad (A9)$$

800      The derivation showing that (A7) and (A8) are equivalent is [given](#) here:

$$\begin{aligned} c_p^{(d)} \theta_v \nabla_\eta \Pi &= c_p^{(d)} \theta_v \nabla_\eta \left( \frac{p}{p_0} \right)^\kappa, \\ &= c_p^{(d)} \theta_v \kappa \left( \frac{p}{p_0} \right)^{\kappa-1} \nabla_\eta \left( \frac{p}{p_0} \right), \\ &= c_p^{(d)} \theta_v \kappa \Pi \left( \frac{p_0}{p} \right) \nabla_\eta \left( \frac{p}{p_0} \right), \\ &= \frac{c_p^{(d)} \theta_v \kappa \Pi}{p} \nabla_\eta p, \\ &= \frac{R^{(d)} \theta_v \Pi}{p} \nabla_\eta p, \\ &= \frac{R^{(d)} T_v}{p} \nabla_\eta p, \\ &= \frac{1}{\rho} \nabla_\eta p. \end{aligned}$$

801 Using the reference states from (Simmons & Jiabin, 1991),

$$\bar{T} = T_0 + T_1 \Pi, \quad (\text{A10})$$

$$\bar{\theta} = T_0 / \Pi + T_1, \quad (\text{A11})$$

802 we can define a geopotential as a function of Exner pressure

$$\bar{\Phi} = -c_p^{(d)} (T_0 \log \Pi + T_1 \Pi - T_1). \quad (\text{A12})$$

803 This "balanced" geopotential obeys

$$c_p^{(d)} \bar{\theta} \nabla \Pi + \nabla \bar{\Phi} = 0 \quad (\text{A13})$$

804 for any Exner pressure. Subtracting this "reference" profile from the PGF yields

$$\begin{aligned} \nabla_\eta \Phi + c_p^{(d)} \theta_v \nabla_\eta \Pi &= \nabla_\eta (\Phi - \bar{\Phi}) + c_p^{(d)} (\theta_v - \bar{\theta}) \nabla_\eta \Pi, \\ &= \nabla_\eta \Phi + c_p^{(d)} \theta_v \nabla_\eta \Pi + c_p^{(d)} T_0 \left[ \nabla_\eta \log \Pi - \frac{1}{\Pi} \nabla_\eta \Pi \right]. \end{aligned} \quad (\text{A14})$$

805 In the continuum, the two formulations (left and right-hand side of (A14)) are identi-  
806 cal. But under discretization, the second formulation can have much less truncation er-  
807 ror.

### 808 A3 Results

809 One year averages of vertical pressure velocity at 500hPa (OMEGA500) have been  
810 found to be a useful quantity to detect spurious up or down-drafts induced by steep orog-  
811 raphy (Figure A1). While the true solution is not known, strong vertical velocities aligned  
812 with element edges that are not found in the CAM-FV reference solution (Figure A1(a))  
813 are likely not physical (spurious). The older CESM2.0 version of SE (Figure A1(d)) us-  
814 ing the "traditional" discretization of the PGF, (A14), exhibits significant spurious noise  
815 patters around steep orography compared to CAM-FV (e.g., around Himalayas and An-  
816 des). This is strongly alleviated by switching to the Exner formulation of the PGF (A8;  
817 Figure A1(c)). By also subtracting reference profiles from pressure-level thickness and  
818 temperature, equations (A5) and (A6) respectively, reduces strong up-down drafts fur-  
819 ther (Figure A1(d)). Switching to the CAM-SE-CSLAM version where physics ten-  
820 dencies are computed on an quasi-equal area physics grid and using the CSLAM transport  
821 scheme, marginal improvements are observed in terms of a smoother vertical velocity field  
822 (Figure A1(e,f)). The configuration shown in Figure A1(d) is used for the simulations  
823 shown in the main text of this paper.

824 It is interesting to note that the noise issues and algorithmic remedies found in the  
825 real-world simulations discussed above, can be investigated by replacing all of physics  
826 with a modified version of the Held-Suarez forcing (Held & Suarez, 1994). The original  
827 formulation of the Held-Suarez idealized test case used a flat Earth ( $\Phi_s = 0$ ) and a dry  
828 atmosphere. By simply adding the surface topography used in 'real-world' simulations  
829 and removing the temperature relaxation in the lower part of domain ( $\sigma > 0.7$ ; see Held  
830 and Suarez (1994) for details), surprisingly realistic vertical velocity fields (in terms of  
831 structure) result (see Figure A2). Since this was a very useful development tool it is shared  
832 in this manuscript.

### 833 Acknowledgments

834 This material is based upon work supported by the National Center for Atmospheric Re-  
835 search (NCAR), which is a major facility sponsored by the NSF under Cooperative Agree-  
836 ment 1852977. Computing and data storage resources, including the Cheyenne super-  
837 computer (Computational and Information Systems Laboratory, 2017), were provided

838 by the Computational and Information Systems Laboratory (CISL) at NCAR. A. Her-  
 839 rington thanks Matt Rehme (NCAR/CISL) for his role in generating the Arctic–GrIS  
 840 visualization available on youtube ([https://www.youtube.com/watch?v=YwHgqDu75s8&t=4s&ab\\_channel=NCARVisLab](https://www.youtube.com/watch?v=YwHgqDu75s8&t=4s&ab_channel=NCARVisLab)).  
 841

842 The data presented in main part of this manuscript is available at <https://github.com/adamrher/2020-arcticgrids>. The source code and data for the Appendix is avail-  
 843 able at <https://github.com/PeterHjortLauritzen/CAM/tree/topo-mods>.  
 844

## 845 References

- 846 Bacmeister, J. T., & Coauthors. (2018). Projected changes in tropical cyclone activ-  
 847 ity under future warming scenarios using a high-resolution climate model. *Cli-*  
 848 *matic Change*, 146, 547–560. Retrieved from <http://dx.doi.org/10.1007/s10584-016-1750-x> doi: 10.1007/s10584-016-1750-x  
 849
- 850 Bacmeister, J. T., Wehner, M. F., Neale, R. B., Gettelman, A., Hannay, C., Lau-  
 851 ritzen, P. H., ... Truesdale, J. E. (2013). Exploratory high-resolution climate  
 852 simulations using the community atmosphere model (cam). *J. Climate*, 27(9),  
 853 3073–3099. doi: 10.1175/JCLI-D-13-00387.1
- 854 Bambach, N. E., Rhoades, A. M., Hatchett, B. J., Jones, A. D., Ullrich, P. A., &  
 855 Zarzycki, C. M. (2021). Projecting climate change in south america using  
 856 variable-resolution community earth system model: An application to chile.  
*International Journal of Climatology*.
- 857 Beljaars, A., Brown, A., & Wood, N. (2004). A new parametrization of turbulent  
 858 orographic form drag. *Quart. J. Roy. Meteor. Soc.*, 130(599), 1327–1347. doi:  
 859 10.1256/qj.03.73
- 860 Bogenschutz, P. A., Gettelman, A., Morrison, H., Larson, V. E., Craig, C., & Scha-  
 861 nen, D. P. (2013). Higher-order turbulence closure and its impact on climate  
 862 simulations in the community atmosphere model. *Journal of Climate*, 26(23),  
 863 9655–9676.
- 864 Box, J. E., Bromwich, D. H., & Bai, L.-S. (2004). Greenland ice sheet surface mass  
 865 balance 1991–2000: Application of polar mm5 mesoscale model and in situ  
 866 data. *Journal of Geophysical Research: Atmospheres*, 109(D16).
- 867 Braithwaite, R. J. (1984). Calculation of degree-days for glacier-climate research.  
*Zeitschrift für Gletscherkunde und Glazialgeologie*, 20(1984), 1–8.
- 868 Burakowski, E. A., Tawfik, A., Ouimette, A., Lepine, L., Zarzycki, C., Novick, K.,  
 869 ... Bonan, G. (2019). Simulating surface energy fluxes using the variable-  
 870 resolution community earth system model (vr-cesm). *Theoretical and Applied  
 871 Climatology*, 138(1), 115–133.
- 872 Calov, R., & Greve, R. (2005). A semi-analytical solution for the positive degree-day  
 873 model with stochastic temperature variations. *Journal of Glaciology*, 51(172),  
 874 173–175.
- 875 Canuto, C., Hussaini, M. Y., Quarteroni, A., & Zang, T. (2007). *Spectral methods:*  
 876 *Evolution to complex geometries and applications to fluid dynamics* (1st ed.).  
 Springer.
- 877 Chang, P., Zhang, S., Danabasoglu, G., Yeager, S. G., Fu, H., Wang, H., ... oth-  
 878 ers (2020). An unprecedented set of high-resolution earth system simulations  
 879 for understanding multiscale interactions in climate variability and change.  
*Journal of Advances in Modeling Earth Systems*, 12(12), e2020MS002298.
- 880 Chepfer, H., Bony, S., Winker, D., Cesana, G., Dufresne, J., Minnis, P., ... Zeng, S.  
 881 (2010). The gcm-oriented calipso cloud product (calipso-goccp). *Journal of  
 882 Geophysical Research: Atmospheres*, 115(D4).
- 883 Collins, W. D., Rasch, P. J., Boville, B. A., Hack, J. J., McCaa, J. R., Williamson,  
 884 D. L., ... Zhang, M. (2006). The formulation and atmospheric simulation  
 885 of the community atmosphere model version 3 (cam3). *Journal of Climate*,

- 890                   19(11), 2144–2161.
- 891 Computational and Information Systems Laboratory. (2017). *Cheyenne: HPE/SGI*  
 892 *ICE XA System (Climate Simulation Laboratory), Boulder, CO: National*  
 893 *Center for Atmospheric Research.* doi: 10.5065/D6RX99HX
- 894 Copernicus, C. (2019). Era5 monthly averaged data on pressure levels from  
 895 1979 to present. URL: <https://cds.climate.copernicus.eu>. doi: 10.24381/  
 896 cds.6860a573
- 897 Craig, C., Bacmeister, J., Callaghan, P., Eaton, B., Gettelman, A., Goldhaber, S. N.,  
 898 ... Vitt, F. M. (2021). *Cam6.3 user's guide* (Tech. Rep.). NCAR/TN-  
 899 571+EDD. doi: 10.5065/Z953-ZC95
- 900 Danabasoglu, G., Lamarque, J.-F., Bacmeister, J., Bailey, D., DuVivier, A., Ed-  
 901 wards, J., ... others (2020). The community earth system model ver-  
 902 sion 2 (cesm2). *Journal of Advances in Modeling Earth Systems*, 12(2),  
 903 e2019MS001916.
- 904 Danielson, J., & Gesch, D. (2011). *Global multi-resolution terrain elevation data*  
 905 *2010 (GMTED2010)* (Open-File Report 2011-1073). U.S. Geological Survey.  
 906 (<http://pubs.usgs.gov/of/2011/1073/pdf/of2011-1073.pdf>)
- 907 Danielson, J. J., & Gesch, D. B. (2011). *Global multi-resolution terrain elevation*  
 908 *data 2010 (GMTED2010)* (Open File Rep. No. 2011-1073). US Geological Sur-  
 909 vey. doi: <https://doi.org/10.3133/ofr20111073>
- 910 Dennis, J., Edwards, J., Evans, K. J., Guba, O., Lauritzen, P. H., Mirin, A. A., ...  
 911 Worley, P. H. (2012). CAM-SE: A scalable spectral element dynamical core for  
 912 the Community Atmosphere Model. *Int. J. High. Perform. C.*, 26(1), 74-89.  
 913 Retrieved from <http://hpc.sagepub.com/content/26/1/74.abstract> doi:  
 914 10.1177/1094342011428142
- 915 Dennis, J., Fournier, A., Spotz, W., St-Cyr, A., Taylor, M., Thomas, S., & Tufo, H.  
 916 (2005). High-resolution mesh convergence properties and parallel efficiency  
 917 of a spectral element atmospheric dynamical core. *ijhpc*, 19, 225-235. doi:  
 918 10.1177/1094342005056108
- 919 Evans, K. J., Kennedy, J. H., Lu, D., Forrester, M. M., Price, S., Fyke, J., ... oth-  
 920 ers (2019). Livvkit 2.1: automated and extensible ice sheet model validation.  
 921 *Geoscientific Model Development*, 12(3), 1067–1086.
- 922 Eyring, V., Bony, S., Meehl, G. A., Senior, C. A., Stevens, B., Stouffer, R. J., &  
 923 Taylor, K. E. (2016). Overview of the coupled model intercomparison project  
 924 phase 6 (cmip6) experimental design and organization. *Geoscientific Model*  
 925 *Development*, 9(5), 1937–1958.
- 926 Fettweis, X., Franco, B., Tedesco, M., Van Angelen, J., Lenaerts, J. T., van den  
 927 Broeke, M. R., & Gallée, H. (2013). Estimating the greenland ice sheet  
 928 surface mass balance contribution to future sea level rise using the regional  
 929 atmospheric climate model mar. *The Cryosphere*, 7(2), 469–489.
- 930 Gettelman, A., Callaghan, P., Larson, V., Zarzycki, C., Bacmeister, J., Lauritzen, P.,  
 931 ... Neale, R. (2017). Regional climate simulations with the community earth  
 932 system model. *J. Adv. Model. Earth Syst.*. (submitted)
- 933 Gettelman, A., Hannay, C., Bacmeister, J. T., Neale, R. B., Pendergrass, A., Dan-  
 934 abasoglu, G., ... others (2019). High climate sensitivity in the community  
 935 earth system model version 2 (cesm2). *Geophysical Research Letters*, 46(14),  
 936 8329–8337.
- 937 Gettelman, A., & Morrison, H. (2015). Advanced two-moment bulk microphysics for  
 938 global models. part i: Off-line tests and comparison with other schemes. *Jour-*  
 939 *nal of Climate*, 28(3), 1268–1287.
- 940 Gettelman, A., Morrison, H., Santos, S., Bogsenschutz, P., & Caldwell, P. (2015).  
 941 Advanced two-moment bulk microphysics for global models. part ii: Global  
 942 model solutions and aerosol–cloud interactions. *Journal of Climate*, 28(3),  
 943 1288–1307.
- 944 Golaz, J.-C., Larson, V. E., & Cotton, W. R. (2002). A pdf-based model for bound-

- 945       ary layer clouds. part i: Method and model description. *Journal of the Atmospheric Sciences*, 59(24), 3540–3551. doi: 10.1175/1520-0469(2002)059<3540:apbmfb>2.0.co;2
- 946       Guba, O., Taylor, M. A., Ullrich, P. A., Overfelt, J. R., & Levy, M. N. (2014). The  
947       spectral element method (sem) on variable-resolution grids: evaluating grid  
948       sensitivity and resolution-aware numerical viscosity. *Geosci. Model Dev.*, 7(6),  
949       2803–2816. doi: 10.5194/gmd-7-2803-2014
- 950       Guo, Z., Wang, M., Qian, Y., Larson, V. E., Ghan, S., Ovchinnikov, M., ... Zhou,  
951       T. (2015). Parametric behaviors of clubb in simulations of low clouds in the c  
952       ommunity atmosphere model (cam). *Journal of Advances in Modeling Earth  
953       Systems*, 7(3), 1005–1025.
- 954       Hansen, N., Simonsen, S. B., Boberg, F., Kittel, C., Orr, A., Souverijns, N., ... Mot-  
955       tram, R. (2022). Brief communication: Impact of common ice mask in surface  
956       mass balance estimates over the antarctic ice sheet. *The Cryosphere*, 16(2),  
957       711–718.
- 958       Held, I. M., & Suarez, M. J. (1994). A proposal for the intercomparison of the dy-  
959       namical cores of atmospheric general circulation models. *Bull. Am. Meteorol.  
960       Soc.*, 73, 1825–1830.
- 961       Herrington, A. R., Lauritzen, P., Taylor, M. A., Goldhaber, S., Eaton, B. E.,  
962       Bacmeister, J., ... Ullrich, P. (2018). Physics-dynamics coupling with element-  
963       based high-order galerkin methods: quasi equal-area physics grid. *Mon. Wea.  
964       Rev.*, 47, 69–84. doi: 10.1175/MWR-D-18-0136.1
- 965       Herrington, A. R., Lauritzen, P. H., Reed, K. A., Goldhaber, S., & Eaton, B. E.  
966       (2019). Exploring a lower resolution physics grid in cam-se-cslam. *Journal of  
967       Advances in Modeling Earth Systems*, 11.
- 968       Herrington, A. R., & Reed, K. A. (2018). An idealized test of the response of the  
969       community atmosphere model to near-grid-scale forcing across hydrostatic  
970       resolutions. *J. Adv. Model. Earth Syst.*, 10(2), 560–575.
- 971       Herrington, A. R., & Reed, K. A. (2020). On resolution sensitivity in the commu-  
972       nity atmosphere model. *Quarterly Journal of the Royal Meteorological Society*,  
973       146(733), 3789–3807.
- 974       Hurrell, J. W., Hack, J. J., Shea, D., Caron, J. M., & Rosinski, J. (2008). A new  
975       sea surface temperature and sea ice boundary dataset for the community at-  
976       mosphere model. *Journal of Climate*, 21(19), 5145–5153.
- 977       Jablonowski, C., & Williamson, D. L. (2011). The pros and cons of diffusion, fil-  
978       ters and fixers in atmospheric general circulation models. In P. H. Lauritzen,  
979       C. Jablonowski, M. Taylor, & R. Nair (Eds.), *Numerical techniques for global  
980       atmospheric models* (pp. 381–493). Berlin, Heidelberg: Springer Berlin Heidel-  
981       berg. doi: 10.1007/978-3-642-11640-7\_13
- 982       Lauritzen, P. H., Bacmeister, J. T., Callaghan, P. F., & Taylor, M. A. (2015). Near  
983       global model topography generation software for unstructured grids. *Geosci-  
984       entific Model Development Discussions*, 8(6), 4623–4651. doi: 10.5194/gmdd-8  
985       -4623-2015
- 986       Lauritzen, P. H., Jablonowski, C., Taylor, M., & Nair, R. D. (2010). Rotated  
987       versions of the jablonowski steady-state and baroclinic wave test cases: A  
988       dynamical core intercomparison. *J. Adv. Model. Earth Syst.*, 2(15), 34 pp.
- 989       Lauritzen, P. H., Mirin, A., Truesdale, J., Raeder, K., Anderson, J., Bacmeister, J.,  
990       & Neale, R. B. (2011). Implementation of new diffusion/filtering operators  
991       in the CAM-FV dynamical core. *Int. J. High Perform. Comput. Appl.*. doi:  
992       10.1177/1094342011410088
- 993       Lauritzen, P. H., Nair, R., Herrington, A., Callaghan, P., Goldhaber, S., Dennis, J.,  
994       ... Dubos, T. (2018). NCAR release of CAM-SE in CESM2.0: A reformula-  
995       tion of the spectral-element dynamical core in dry-mass vertical coordinates  
996       with comprehensive treatment of condensates and energy. *J. Adv. Model.  
997       Earth Syst.*, 10(7), 1537–1570. doi: 10.1029/2017MS001257

- 1000 Lauritzen, P. H., Taylor, M. A., Overfelt, J., Ullrich, P. A., Nair, R. D., Goldhaber,  
 1001 S., & Kelly, R. (2017). CAM-SE-CSLAM: Consistent coupling of a conser-  
 1002 vative semi-lagrangian finite-volume method with spectral element dynamics.  
 1003 *Mon. Wea. Rev.*, 145(3), 833–855. doi: 10.1175/MWR-D-16-0258.1
- 1004 Lawrence, D. M., Fisher, R. A., Koven, C. D., Oleson, K. W., Swenson, S. C., Bo-  
 1005 nan, G., ... others (2019). The community land model version 5: Description  
 1006 of new features, benchmarking, and impact of forcing uncertainty. *Journal of*  
 1007 *Advances in Modeling Earth Systems*, 11(12), 4245–4287.
- 1008 Lin, S.-J. (2004). A 'vertically Lagrangian' finite-volume dynamical core for global  
 1009 models. *Mon. Wea. Rev.*, 132, 2293–2307.
- 1010 Lin, S.-J., & Rood, R. B. (1997). An explicit flux-form semi-Lagrangian shallow-  
 1011 water model on the sphere. *Q.J.R.Meteorol.Soc.*, 123, 2477–2498.
- 1012 Lipscomb, W. H., Fyke, J. G., Vizcaíno, M., Sacks, W. J., Wolfe, J., Vertenstein,  
 1013 M., ... Lawrence, D. M. (2013). Implementation and initial evaluation of the  
 1014 glimmer community ice sheet model in the community earth system model.  
 1015 *Journal of Climate*, 26(19), 7352–7371.
- 1016 Loeb, N. G., Doelling, D. R., Wang, H., Su, W., Nguyen, C., Corbett, J. G., ...  
 1017 Kato, S. (2018). Clouds and the earth's radiant energy system (ceres) energy  
 1018 balanced and filled (ebaf) top-of-atmosphere (toa) edition-4.0 data product.  
 1019 *Journal of Climate*, 31(2), 895–918.
- 1020 Lofverstrom, M., Fyke, J. G., Thayer-Calder, K., Muntjewerf, L., Vizcaino, M.,  
 1021 Sacks, W. J., ... Bradley, S. L. (2020). An efficient ice sheet/earth sys-  
 1022 tem model spin-up procedure for cesm2-cism2: Description, evaluation, and  
 1023 broader applicability. *Journal of Advances in Modeling Earth Systems*, 12(8),  
 1024 e2019MS001984.
- 1025 Morlighem, M., Rignot, E., Mouginot, J., Seroussi, H., & Larour, E. (2014). Deeply  
 1026 incised submarine glacial valleys beneath the greenland ice sheet. *Nature Geo-  
 1027 science*, 7(6), 418–422.
- 1028 Mottram, R., Boberg, F., Langen, P., Yang, S., Rodehacke, C., Christensen, J. H.,  
 1029 & Madsen, M. S. (2017). Surface mass balance of the greenland ice sheet in  
 1030 the regional climate model hirham5: Present state and future prospects. *Low  
 1031 Temp. Sci.*, 75, 105–115.
- 1032 Muntjewerf, L., Sacks, W. J., Lofverstrom, M., Fyke, J., Lipscomb, W. H., Er-  
 1033 nani da Silva, C., ... Sellevold, R. (2021). Description and Demonstration of  
 1034 the Coupled Community Earth System Model v2–Community Ice Sheet Model  
 1035 v2 (CESM2-CISM2). *Journal of Advances in Modeling Earth Systems*, 13(6),  
 1036 e2020MS002356.
- 1037 Neale, R. B., Richter, J. H., & Jochum, M. (2008). The impact of convection on  
 1038 ENSO: From a delayed oscillator to a series of events. *J. Climate*, 21, 5904–  
 1039 5924.
- 1040 Noël, B., Van De Berg, W., Van Meijgaard, E., Kuipers Munneke, P., Van De Wal,  
 1041 R., & Van Den Broeke, M. (2015). Evaluation of the updated regional climate  
 1042 model racmo2. 3: summer snowfall impact on the greenland ice sheet. *The  
 1043 Cryosphere*, 9(5), 1831–1844.
- 1044 Noël, B., van de Berg, W. J., Lhermitte, S., & van den Broeke, M. R. (2019). Rapid  
 1045 ablation zone expansion amplifies north greenland mass loss. *Science advances*,  
 1046 5(9), eaaw0123.
- 1047 Noël, B., van de Berg, W. J., Van Wessem, J. M., Van Meijgaard, E., Van As, D.,  
 1048 Lenaerts, J., ... others (2018). Modelling the climate and surface mass bal-  
 1049 ance of polar ice sheets using racmo2–part 1: Greenland (1958–2016). *The  
 1050 Cryosphere*, 12(3), 811–831.
- 1051 Obrien, T. A., Collins, W. D., Kashinath, K., Rübel, O., Byna, S., Gu, J., ...  
 1052 Ullrich, P. A. (2016). Resolution dependence of precipitation statistical  
 1053 fidelity in hindcast simulations. *J. Adv. Model. Earth Syst.*, 8(2), 976–  
 1054 990. Retrieved from <http://dx.doi.org/10.1002/2016ms000671> doi:

- 1055 10.1002/2016ms000671
- 1056 Ohmura, A. (2001). Physical basis for the temperature-based melt-index method.  
 1057 *Journal of applied Meteorology*, 40(4), 753–761.
- 1058 Pfister, G. G., Eastham, S. D., Arellano, A. F., Aumont, B., Barsanti, K. C., Barth,  
 1059 M. C., ... others (2020). The multi-scale infrastructure for chemistry and  
 1060 aerosols (musica). *Bulletin of the American Meteorological Society*, 101(10),  
 1061 E1743–E1760.
- 1062 Pollard, D. (2010). A retrospective look at coupled ice sheet–climate modeling. *Cli-  
 1063 matic Change*, 100(1), 173–194.
- 1064 Pollard, D., & Groups, P. P. (2000). Comparisons of ice-sheet surface mass budgets  
 1065 from paleoclimate modeling intercomparison project (pmip) simulations. *Global  
 1066 and Planetary Change*, 24(2), 79–106.
- 1067 Pope, V., & Stratton, R. (2002). The processes governing horizontal resolution sensi-  
 1068 tivity in a climate model. *Climate Dynamics*, 19(3-4), 211–236.
- 1069 Putman, W. M., & Lin, S.-J. (2007). Finite-volume transport on various cubed-  
 1070 sphere grids. *J. Comput. Phys.*, 227(1), 55–78.
- 1071 Rae, J., Adalgeirsdóttir, G., Edwards, T. L., Fettweis, X., Gregory, J., Hewitt, H.,  
 1072 ... others (2012). Greenland ice sheet surface mass balance: evaluating simu-  
 1073 lations and making projections with regional climate models. *The Cryosphere*,  
 1074 6(6), 1275–1294.
- 1075 Rasch, P. J., & Williamson, D. L. (1990). Computational aspects of moisture trans-  
 1076 port in global models of the atmosphere. *Q. J. R. Meteorol. Soc.*, 116, 1071–  
 1077 1090.
- 1078 Reeh, N. (1991). Parameterization of melt rate and surface temperature in the  
 1079 greenland ice sheet. *Polarforschung*, 59(3), 113–128.
- 1080 Rhoades, A. M., Huang, X., Ullrich, P. A., & Zarzycki, C. M. (2016). Characterizing  
 1081 sierra nevada snowpack using variable-resolution cesm. *Journal of Applied Me-  
 1082 teorology and Climatology*, 55(1), 173–196. Retrieved from <https://doi.org/10.1175/JAMC-D-15-0156.1> doi: 10.1175/JAMC-D-15-0156.1
- 1083 Richter, J. H., Sassi, F., & Garcia, R. R. (2010). Toward a physically based gravity  
 1084 wave source parameterization in a general circulation model. *J. Atmos. Sci.*,  
 1085 67, 136–156. doi: dx.doi.org/10.1175/2009JAS3112.1
- 1086 Rignot, E., & Mouginot, J. (2012). Ice flow in greenland for the international polar  
 1087 year 2008–2009. *Geophysical Research Letters*, 39(11).
- 1088 Roeckner, E., Brokopf, R., Esch, M., Giorgetta, M., Hagemann, S., Kornblueh, L.,  
 1089 ... Schulzweida, U. (2006). Sensitivity of simulated climate to horizontal  
 1090 and vertical resolution in the echam5 atmosphere model. *Journal of Climate*,  
 1091 19(16), 3771–3791.
- 1092 Sellevold, R., Van Kampenhout, L., Lenaerts, J., Noël, B., Lipscomb, W. H., &  
 1093 Vizcaino, M. (2019). Surface mass balance downscaling through elevation  
 1094 classes in an earth system model: Application to the greenland ice sheet. *The  
 1095 Cryosphere*, 13(12), 3193–3208.
- 1096 Serreze, M. C., Barrett, A. P., Slater, A. G., Steele, M., Zhang, J., & Trenberth,  
 1097 K. E. (2007). The large-scale energy budget of the arctic. *Journal of Geophysi-  
 1098 cal Research: Atmospheres*, 112(D11).
- 1099 Simmons, A. J., & Jiabin, C. (1991). The calculation of geopotential and  
 1100 the pressure gradient in the ECMWF atmospheric model: Influence on  
 1101 the simulation of the polar atmosphere and on temperature analyses.  
 1102 *Quart. J. Roy. Meteor. Soc.*, 117(497), 29–58. Retrieved from <https://rmetts.onlinelibrary.wiley.com/doi/abs/10.1002/qj.49711749703> doi:  
 1103 <https://doi.org/10.1002/qj.49711749703>
- 1104 Small, R. J., Bacmeister, J., Bailey, D., Baker, A., Bishop, S., Bryan, F., ... Verten-  
 1105 stein, M. (2014). A new synoptic scale resolving global climate simulation  
 1106 using the community earth system model. *J. Adv. Model. Earth Syst.*, 6(4),  
 1107 1065–1094. doi: 10.1002/2014MS000363

- 1110 Suarez, M. J., & Takacs, L. L. (1995). Volume 5 documentation of the aries/geos dy-  
 1111 namical core: Version 2.
- 1112 Taylor, M. A., & Fournier, A. (2010). A compatible and conservative spectral el-  
 1113 ement method on unstructured grids. *J. Comput. Phys.*, 229(17), 5879 - 5895.  
 1114 doi: 10.1016/j.jcp.2010.04.008
- 1115 Taylor, M. A., Guba, O., Steyer, A., Ullrich, P. A., Hall, D. M., & Eldred, C.  
 1116 (2020). An energy consistent discretization of the nonhydrostatic equations  
 1117 in primitive variables. *Journal of Advances in Modeling Earth Systems*, 12(1).  
 1118 doi: 10.1029/2019MS001783
- 1119 Taylor, M. A., Tribbia, J., & Iskandarani, M. (1997). The spectral element method  
 1120 for the shallow water equations on the sphere. *J. Comput. Phys.*, 130, 92-108.
- 1121 Team, E. J. S., Balaji, V., Boville, B., Collins, N., Craig, T., Cruz, C., ... others  
 1122 (2021). *Esmf user guide* (Tech. Rep.).
- 1123 Ullrich, P. A., & Taylor, M. A. (2015). Arbitrary-order conservative and consis-  
 1124 tent remapping and a theory of linear maps: Part i. *Monthly Weather Review*,  
 1125 143(6), 2419–2440.
- 1126 Ullrich, P. A., Zarzycki, C. M., McClenny, E. E., Pinheiro, M. C., Stansfield, A. M.,  
 1127 & Reed, K. A. (2021). Tempestextremes v2. 1: a community framework for  
 1128 feature detection, tracking and analysis in large datasets. *Geoscientific Model  
 1129 Development Discussions*, 1–37.
- 1130 Van Angelen, J., Lenaerts, J., Lhermitte, S., Fettweis, X., Kuipers Munneke, P.,  
 1131 Van den Broeke, M., ... Smeets, C. (2012). Sensitivity of greenland ice  
 1132 sheet surface mass balance to surface albedo parameterization: a study with a  
 1133 regional climate model. *The Cryosphere*, 6(5), 1175–1186.
- 1134 van Kampenhout, L., Lenaerts, J. T., Lipscomb, W. H., Lhermitte, S., Noël, B.,  
 1135 Vizcaíno, M., ... van den Broeke, M. R. (2020). Present-day greenland ice  
 1136 sheet climate and surface mass balance in cesm2. *Journal of Geophysical  
 1137 Research: Earth Surface*, 125(2).
- 1138 van Kampenhout, L., Rhoades, A. M., Herrington, A. R., Zarzycki, C. M., Lenaerts,  
 1139 J. T. M., Sacks, W. J., & van den Broeke, M. R. (2018). Regional grid refine-  
 1140 ment in an earth system model: Impacts on the simulated greenland surface  
 1141 mass balance. *The Cryosphere Discuss..* doi: 10.5194/tc-2018-257
- 1142 Wan, H., Giorgetta, M. A., Zängl, G., Restelli, M., Majewski, D., Bonaventura, L.,  
 1143 ... others (2013). "the icon-1.2 hydrostatic atmospheric dynamical core on  
 1144 triangular grids, part i: formulation and performance of the baseline version".  
*Geosci. Model Dev.*, 6, 735–763.
- 1145 Williamson, D. (2007). The evolution of dynamical cores for global atmospheric  
 1146 models. *J. Meteor. Soc. Japan*, 85, 241-269.
- 1147 Williamson, D. (2008). Convergence of aqua-planet simulations with increasing res-  
 1148 olution in the community atmospheric model, version 3. *Tellus A*, 60(5), 848–  
 1149 862. doi: 10.1111/j.1600-0870.2008.00339.x
- 1150 Zarzycki, C. M., Jablonowski, C., & Taylor, M. A. (2014). Using variable-resolution  
 1151 meshes to model tropical cyclones in the community atmosphere model. *Mon.  
 1152 Wea. Rev.*, 142(3), 1221-1239. doi: 10.1175/MWR-D-13-00179.1
- 1153 Zhang, G., & McFarlane, N. (1995). Sensitivity of climate simulations to the  
 1154 parameterization of cumulus convection in the canadian climate center general-  
 1155 circulation model. *ATMOSPHERE-OCEAN*, 33(3), 407-446.

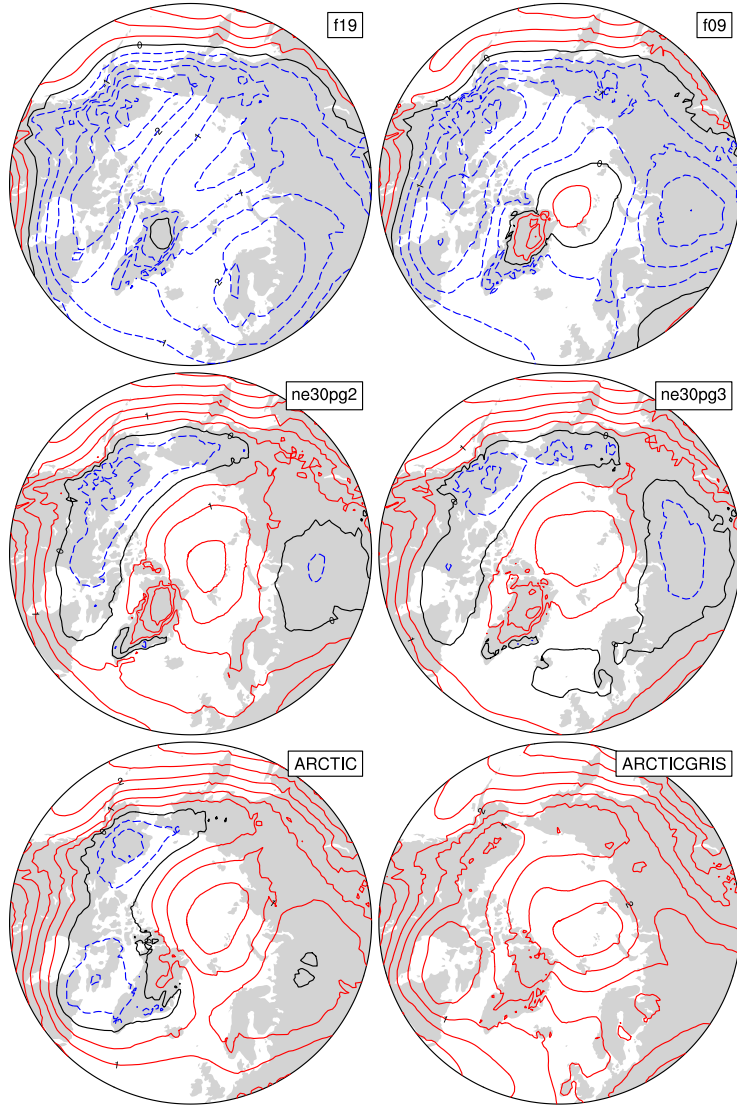


**Figure 6.** 1979-1998 lower troposphere, northern hemisphere summer virtual temperature biases, computed as the difference from ERA5. Lower troposphere layer mean virtual temperature is derived from the 1000 hPa - 500h Pa geopotential thickness, using the hypsometric equation. Differences are computed after mapping the ERA5 data to the finite-volume grids since the geopotential field is only available on the output tapes in the spectral-element runs that have been interpolated to the f09 grid, inline.

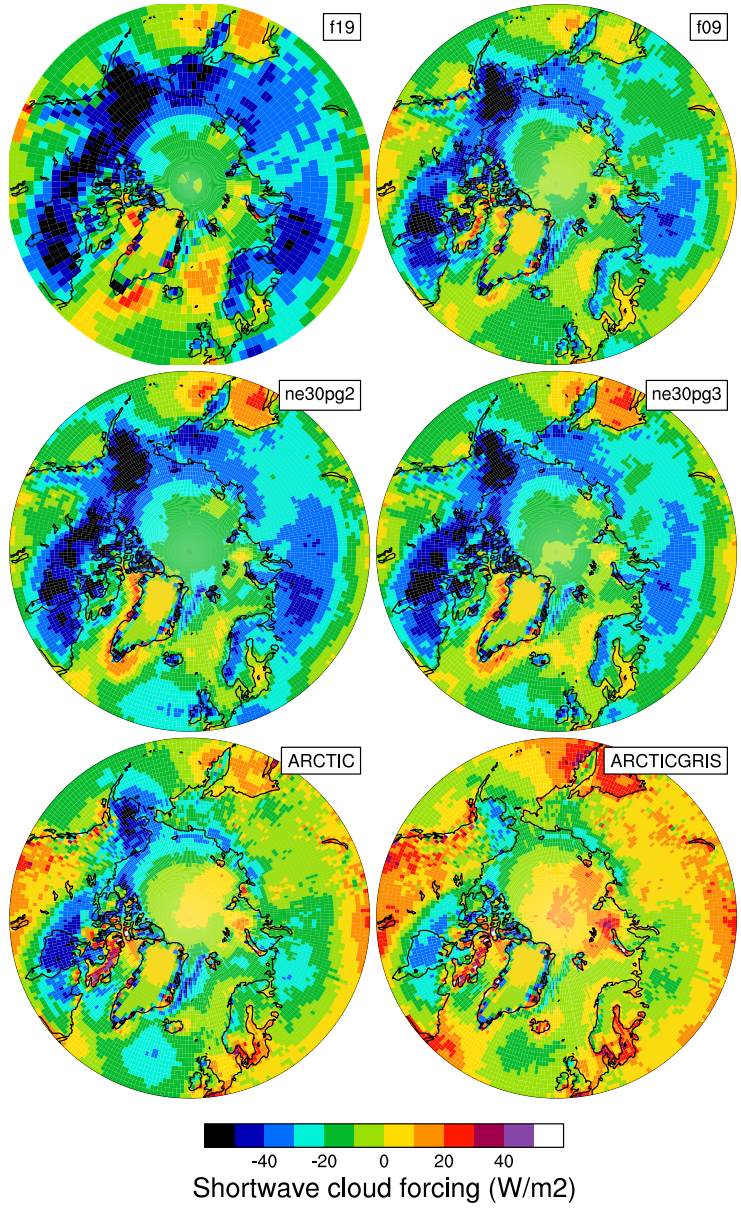


**Figure 7.** 1979-1998 Northern Hemisphere summer shortwave cloud forcing bias, relative to the CERES-EBAF gridded dataset. Shortwave cloud forcing is defined as the difference between all-sky and clear-sky net shortwave fluxes at the top of the atmosphere. Differences are computed after mapping all model output to the 1° CERES-EBAF grid.

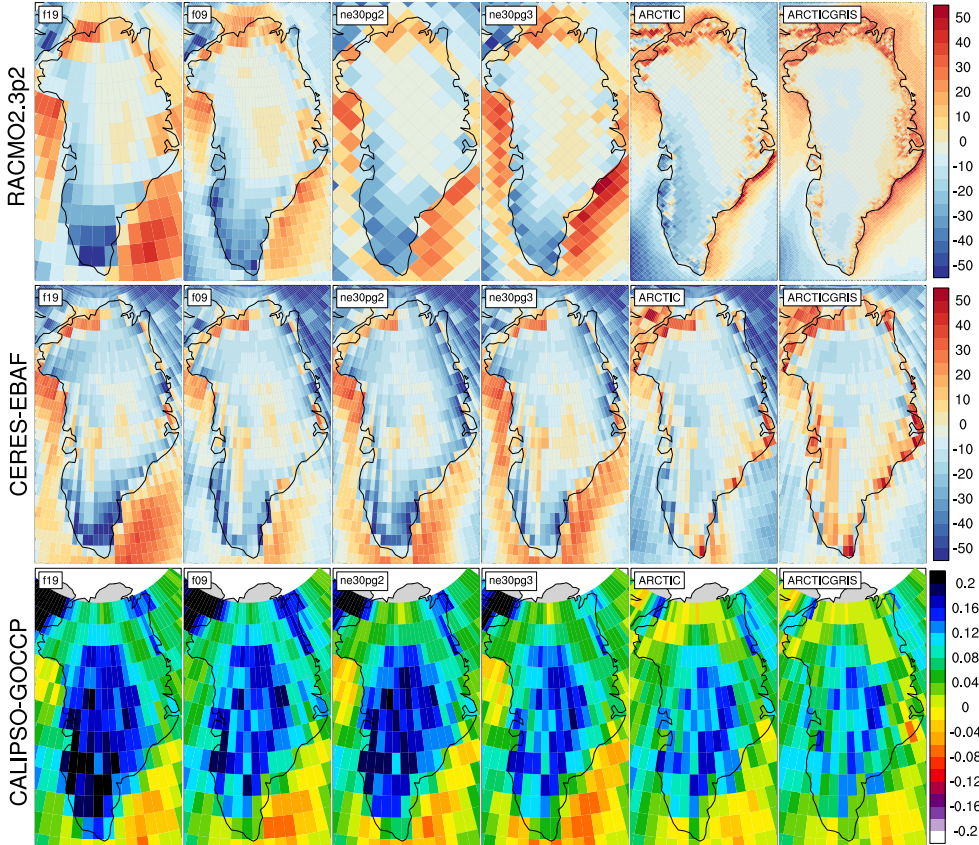


**Figure 8.** 1979-1998 northern hemisphere summer surface incident shortwave radiation bias ( $\text{W}/\text{m}^2$ ), computed as the difference (top) from CERES, and (middle) RACMO2.3p2 dataset, and the (bottom) total cloud fraction bias relative to the CALIPSO dataset. CALIPSO and CERES differences are found by mapping the model output to the  $1^\circ$  grid, and differences in the bottom panel are computed after mapping the RACMO2.3p2 dataset to the individual model grids. Note that the averaging period for the CALIPSO-GOCCP and CERES-EBAF panels, 2006-2017 and 2003-2020, respectively, are different from the averaging period for the model results.

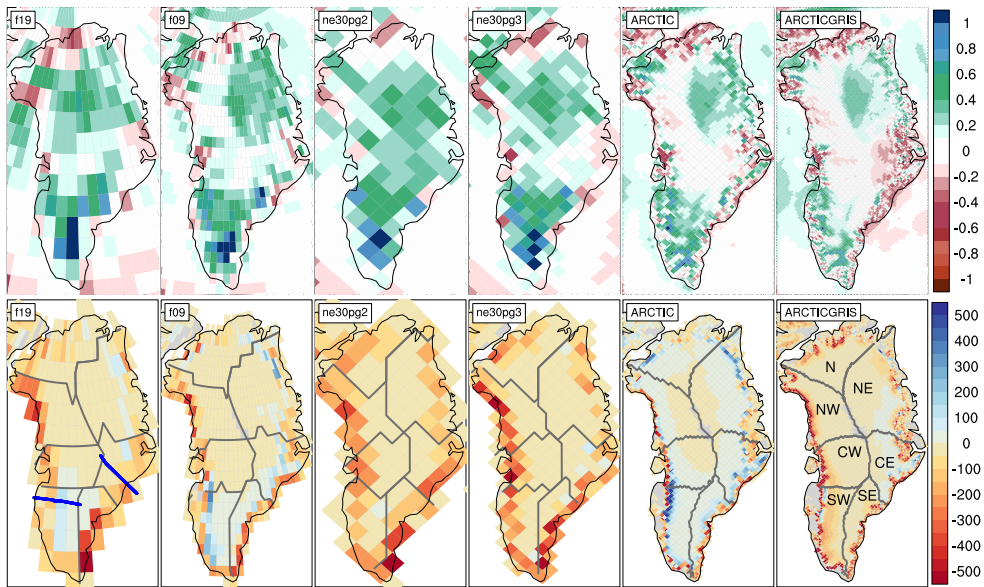


**Figure 9.** 1979-1998 (top) annual precipitation and (bottom) ice/snow melt biases relative to RACMO2.3p2, evaluated on the native model grids. The precipitation biases are expressed as fractional changes, whereas the melt biases are absolute changes (mm/yr). In the bottom panel, the Rignot and Mouginot (2012) basin boundaries are shown in grey for each model grid. Note that Figure 11 uses the basin boundaries for the two common ice masks, shown in the f19 and ne30pg2 panels, in computing the basin-scale integrals. Blue lines in the f19 panel show the location of the two transects plotted in Figure 12..

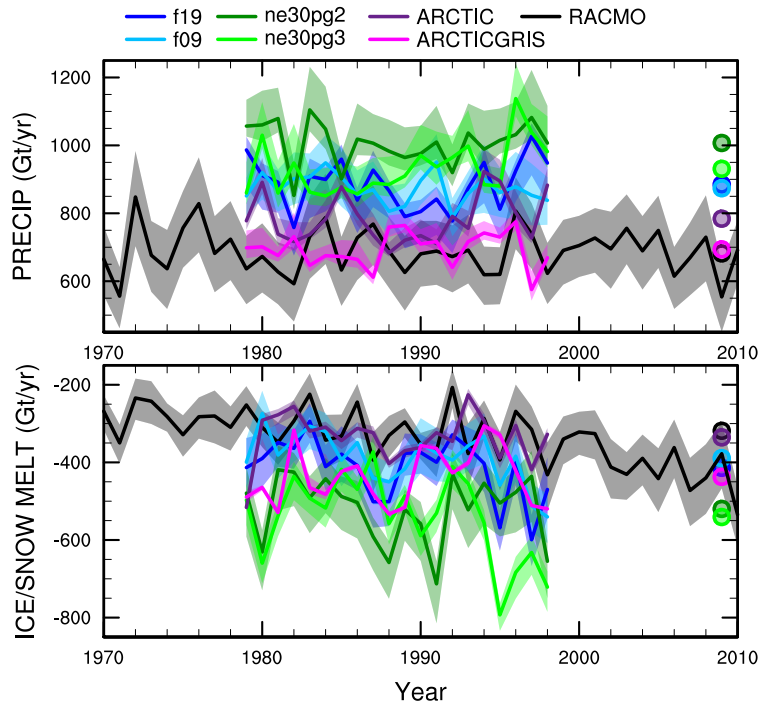


**Figure 10.** Time-series of annual (solid+liquid) precipitation (top) and annual runoff (bottom) integrated over the Greenland Ice Sheet for all six simulations and compared to the RACMO datasets. The time-series were generated using the common ice mask approach, which results in up to 4 ensembles, with the mean value given by the solid line and shading spanning the extent of the ensemble members.

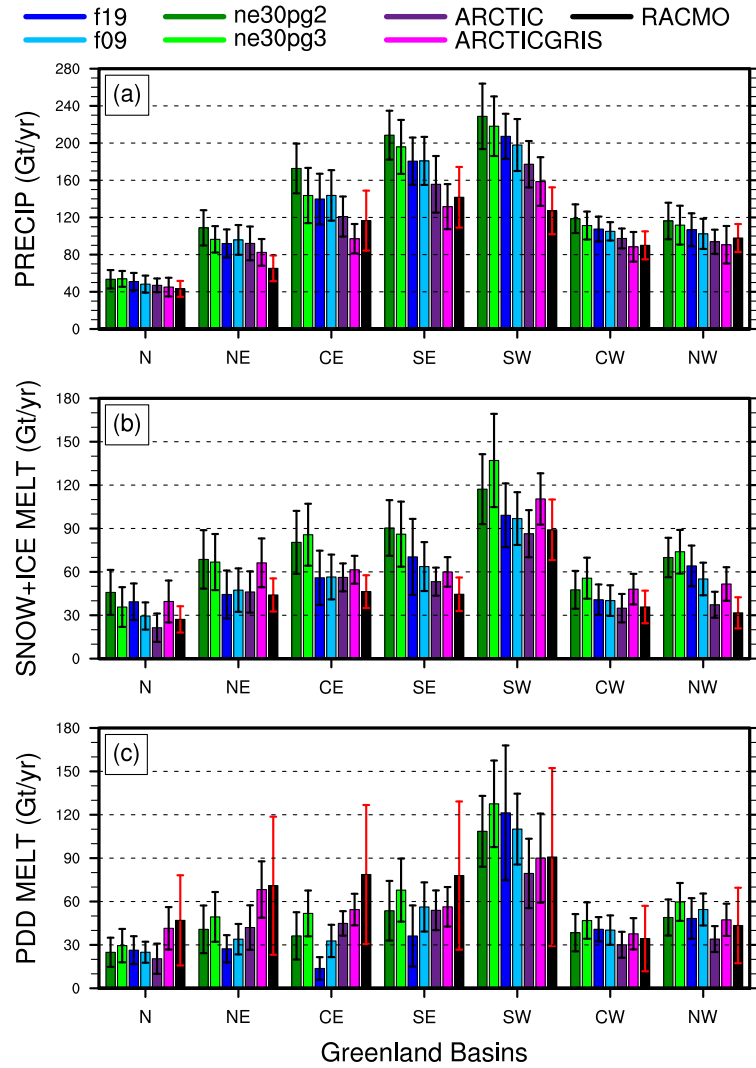


**Figure 11.** 1979–1998 basin integrated components of the SMB; (top) precipitation, (middle) ice/snow melt and (bottom) ice/snow melt estimated from the PDD method. Whiskers span the max/min of the four ensemble members generated from the common-ice-mask approach. Basin definitions are after Rignot and Mouginot (2012), and are found on the common ice masks using a nearest neighbor approach, and shown in Figure 9.

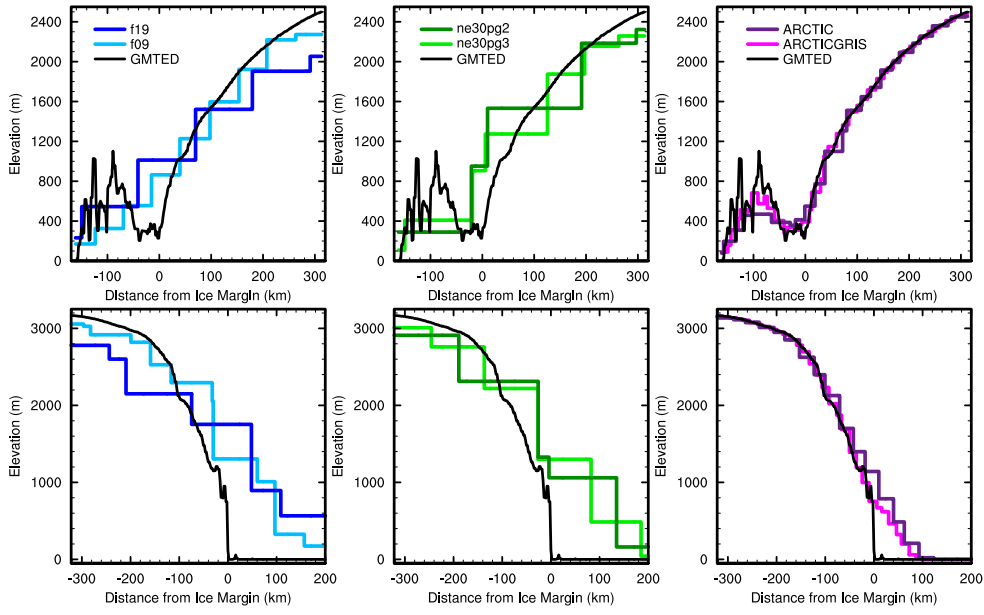


**Figure 12.** Model surface elevation along the (top) K-transect, and (bottom) a transect spanning the central dome down to the Kangerlussuaq glacier in southeast Greenland, for all model grids. The GMTED reference surface is a 1 km surface elevation dataset (J. Danielson & Gesch, 2011) used for generating the CAM topographic boundary conditions.

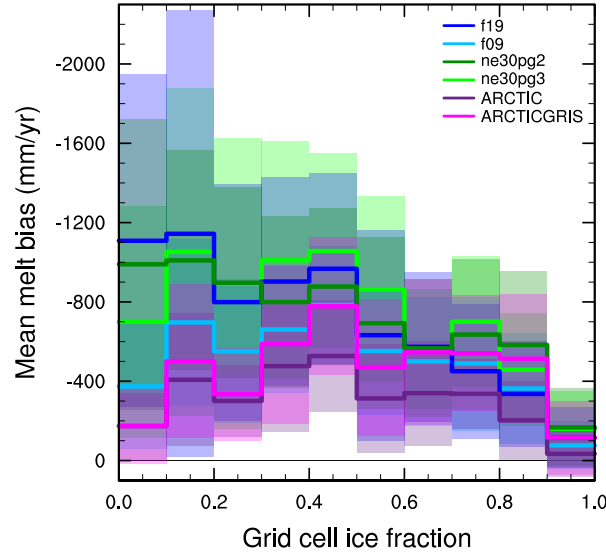


**Figure 13.** Fractional melt bias over the GrIS, computed relative to the RACMO datasets using the common ice mask approach, and conditionally sampled by grid cell ice fraction provided by the common ice masks. Solid lines are the mean of the distribution with  $\pm$  one standard deviation expressed by shading.

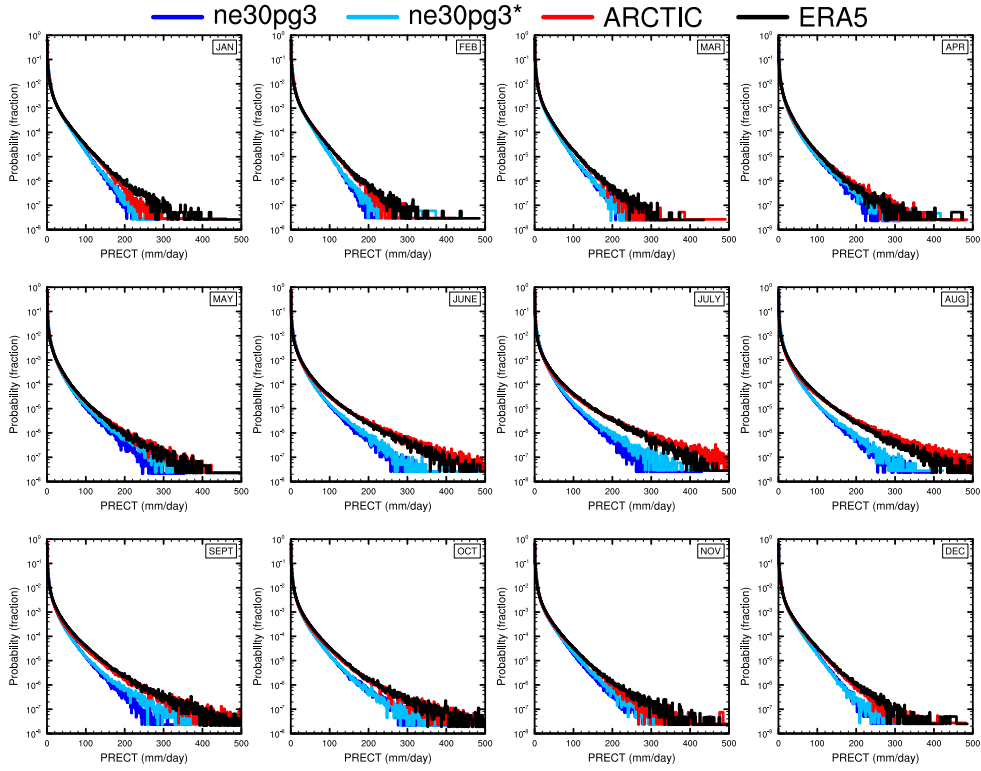


**Figure 14.** PDFs of the total precipitation rate associated with tracked storms, by month, in the ne30pg3, ne30pg3\* and Arctic runs, and compared with the ERA5 dataset.

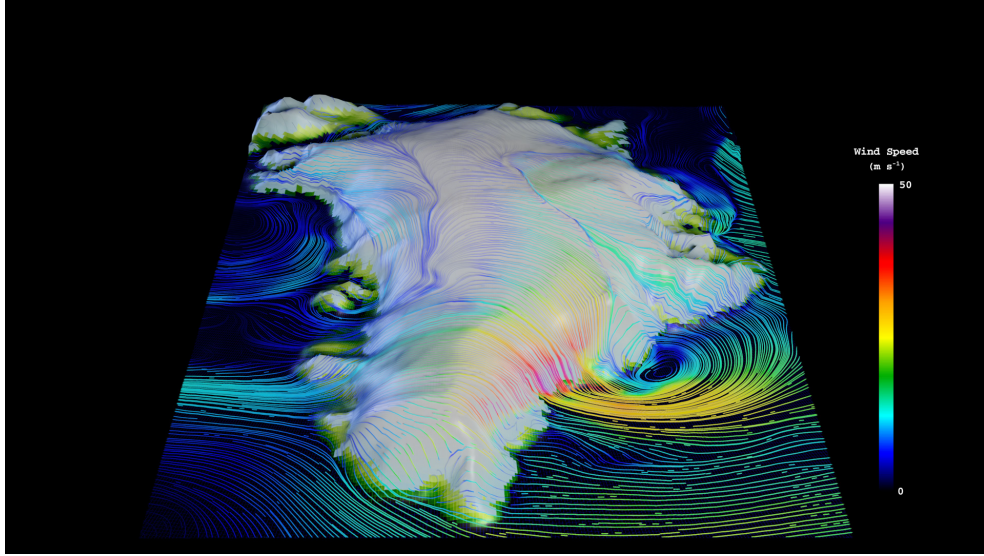


**Figure 15.** Snapshot of the lowest model level streamlines from the Arctic – GrIS visualization, with color shading denoting the wind magnitude.

## OMEGA500, 1 year average, F2000climo, 32 levels

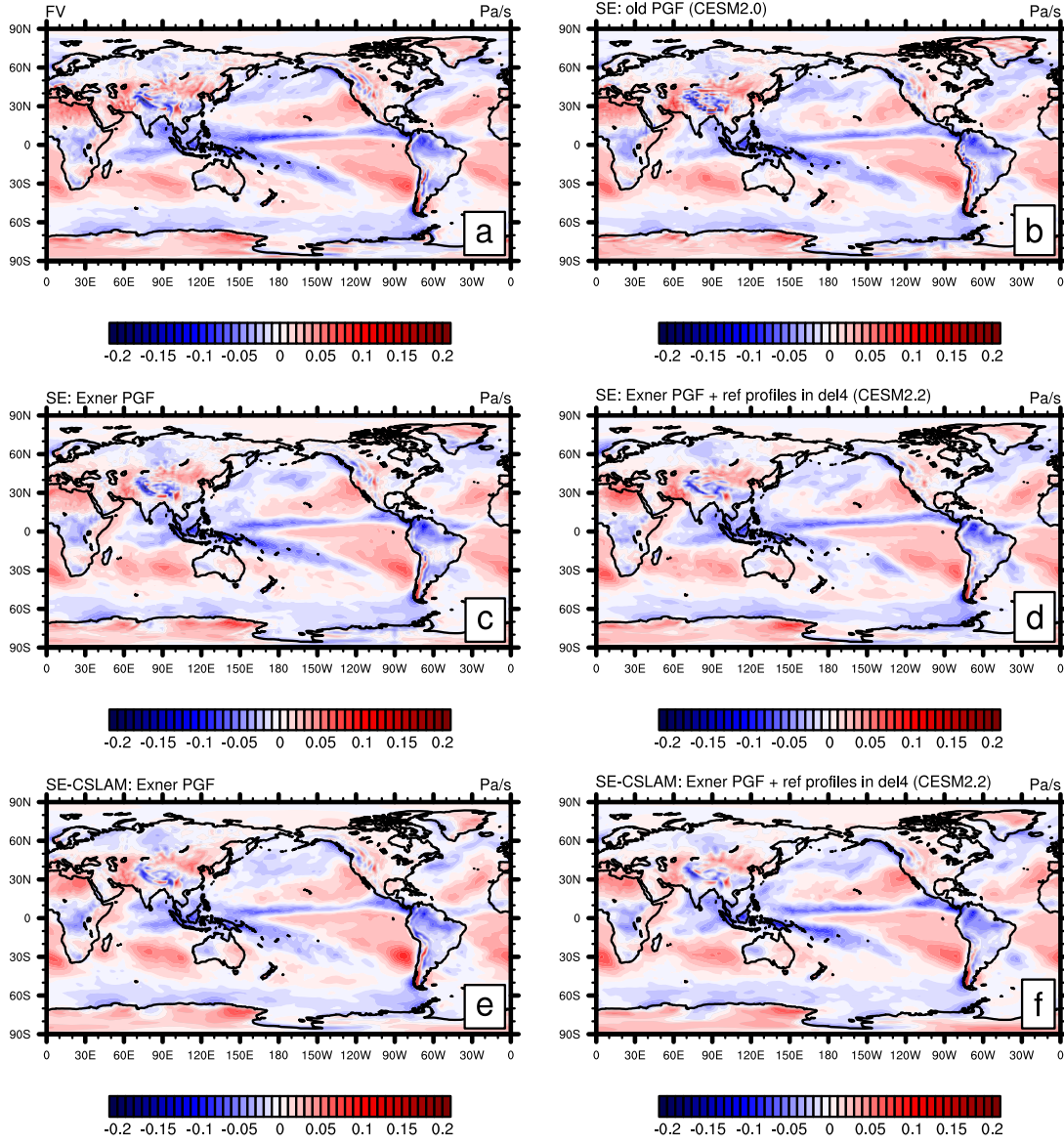


**Figure A1.** One year averages of vertical pressure velocity at 500hPa (**OMEGA500**) using (a) CAM-FV (Finite-Volume dynamical core) and (b-f) various versions of the spectral-element (SE) dynamical core at approximately  $1^{\circ}$  horizontal resolution and using 32 levels. (b) is equivalent to the CESM2.0 version of the SE dynamical core using the "traditional"/"old" discretization of the pressure-gradient force (PGF). Plot (c) is equivalent to configuration (b) but using the Exner form of the PGF. Plot (d) is the same as configuration (c) but also subtracting reference profiles from pressure and temperature before applying hyperviscosity operators (which is equivalent to the CESM2.2 version of SE in terms of the dynamical core). Plots (e) and (f) are equivalent to (c) and (d), respectively, by using the SE-CSLAM (`ne30pg3`) version of the SE dynamical core (i.e. separate quasi-uniform physics grid and CSLAM transport scheme).

OMEGA500, 18 months average, FHS94 forcing, 32 levels

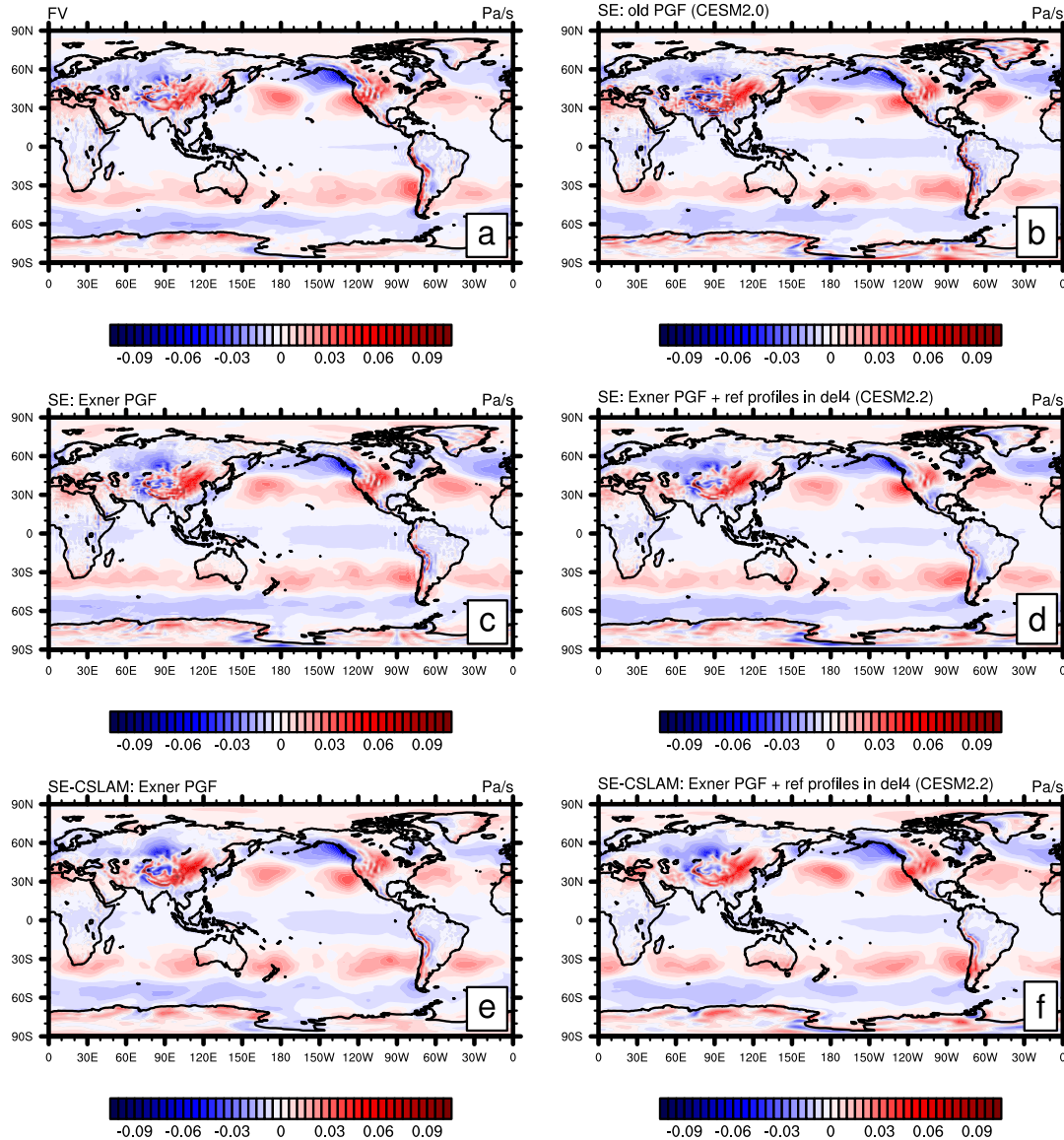


**Figure A2.** Same as Figure A1 but using modified Held-Suarez forcing and the average is over 18 months (excl. spin-up).